Amyloid beta precursor protein contributes to brain aging and learning decline in short-lived turquoise killifish (*Nothobranchius furzeri*)

Dennis E.M. de Bakker[a,b,c,d], Mihaela Mihaljević[b], Kunal Gharat[a], Yasmin Richter[e], Sara Bagnoli[f], Frauke van Bebber[g], Lisa Adam[a], Farzana Shamim-Schulze[a], Oliver Ohlenschläger[a], Martin Bens[a], Emilio Cirri[a], Adam Antebi[b,h], Ivan Matić[b,h], Anja Schneider[i], Bettina Schmid[g], Alessandro Cellerino[a,f], Janine Kirstein[a,e], Dario Riccardo Valenzano[a,b,c,d,*]

[a]Leibniz Institute on Aging – Fritz Lipmann Institute (FLI), Beutenbergstrasse 11, 07745, Jena, Germany;
[b]Max Planck Institute for Biology of Ageing, Joseph-Stelzmann-Straße 9B, 50931 Cologne, Germany;
[c]Cluster of Excellence "Balance of the Microverse", Friedrich-Schiller-University, Jena, Germany;
[d]Jena University Hospital/Friedrich-Schiller-University, Jena, Germany.
[e]Friedrich-Schiller-University, Institute for Biochemistry and Biophysics, Hans-Knöll-Str. 2, 07745, Jena, Germany
[f]Scuola Normale Superiore, Piazza dei Cavalieri, 7, 56126 Pisa PI, Italy;
[g]German Center for Neurodegenerative Diseases Munich, Feodor-Lynen-Str. 17, 81377, München, Germany;
[h]Cologne Excellence Cluster on Cellular Stress Responses in Aging-Associated Diseases (CECAD); University of Cologne, 50931, Cologne, Germany;
[i]German Center for Neurodegenerative Diseases, Venusberg-Campus 1/99, 53127 Bonn, Germany;

*corresponding author: dvalenzano@leibniz-fli.de

Abstract

Brain aging is a pivotal risk factor for many neurodegenerative diseases, yet its molecular and cellular mechanisms remain elusive. The amyloid-beta precursor protein (APP) is among the most studied proteins linked to brain pathology; however, its role in non-pathological brain aging remains poorly characterized. Here, we investigate the natural impact of APP on normal brain aging using the short-lived turquoise killifish (*Nothobranchius furzeri*), which exhibits rapid and spontaneous age-related decline. We found that pyroglutamated amyloid beta —a neurotoxic Aβ variant—accumulates intra-neuronally in an age-dependent manner, co-localizing with a marker of cell death. We found that intraneuronal pyroglutamated amyloid beta is also present in old human brains, suggesting deep evolutionary conservation. To determine Aβ's role in spontaneous brain aging, we generated an "amyloid precursor protein a" (*appa*) knock-out killifish line using CRISPR/Cas9. The knock-out of *appa* rescued age-dependent increase in cell death and inflammation, mitigated proteome-wide brain aging and improved the age-related decline in neuronal activity and learning capacity. Our findings show a key role for Aβ precursor protein in non-pathological brain aging, making it a suitable target for anti-aging interventions.

54 **Introduction**

55

56 The aging brain undergoes several changes, including protein aggregation, inflammation, and neuronal
57 degeneration, which is associated with a decline in cognitive capacity. These changes are often
58 exacerbated during neurodegenerative diseases, which possibly represent alternative aging trajectories[1–3].
59 Amyloid beta (Aβ) is a highly studied peptide that aggregates in the brain of normal – i.e., non-
60 pathological – aging individuals as well as Alzheimer's disease (AD) patients[4,5]. Genetic and
61 pharmacological induction of Aβ can drive neurodegenerative symptoms in worms[6,7], flies[8,9] and mice[10–
62 12], and monoclonal antibodies and vaccination strategies targeting Aβ are being developed to slow down
63 cognitive decline in AD patients[13–18]. However, whether Aβ plays a key role in normal aging and whether
64 it can be targeted to reduce the degenerative brain phenotypes of the normal aging brain remains largely
65 unexplored.

66

67 The investigation of the effect of spontaneous Aβ accumulation during aging requires an animal model
68 whose natural aging trajectory includes both Aβ accumulation, as well as neurodegenerative phenotypes.
69 Therefore, we set out to investigate the Aβ dynamics in a naturally short-lived vertebrate, which displays
70 robust brain aging phenotypes, the turquoise killifish (*Nothobranchius furzeri*)[3]. Turquoise killifish have a
71 median lifespan between three and eight months and rapidly develop a range of age-related phenotypes
72 overlapping with human aging. These phenotypes include sarcopenia[19], cancer susceptibility[20], telomere
73 attrition[21,22], impaired regenerative capacity[23,24], as well as a decrease in antibody diversity and increased
74 immunosenescence[25–27]. Meanwhile, the killifish brain is subjected to age-related protein aggregation[28–33],
75 astrogliosis[34,35], inflammation[24,28,35,36], neuronal degeneration[29,37–39] and reduced neurogenic
76 potential[24,34,35], which together might underlie a decreased learning capacity[39–41]. Considering that these
77 brain aging phenotypes arise spontaneously, the turquoise killifish has been proposed as a promising
78 model to study spontaneous neurodegenerative processes within the context of aging[3,42].

79

80 Here, we investigate the role of Aβ in normal brain aging. Using transcriptomics, proteomics, and
81 immunohistochemistry, we show that with age, the killifish brain becomes subjected to a robust
82 inflammatory state accompanied by accumulation of pyroglutamated Aβ, a post-translationally modified
83 and particularly toxic Aβ variant[43,44]. Finally, we show that knocking out the *appa* isoform of the Aβ
84 precursor genes mitigates age-related brain phenotypes.
85
86
87
88
89
90
91
92
93
94

Results

Amyloid beta is evolutionary conserved between humans and turquoise killifish and is expressed in the aged turquoise killifish brain

The turquoise killifish is a naturally short-lived species, reaching sexual maturity within 3 to 5 weeks post-hatching. In this study, we define killifish (strain ZMZ1001) as "young," "aged," and "old" based on their ages of 6 weeks, 6 months, and 9 months, respectively. These age categories correspond to survival rates of 100%, 89%, and 44% (**Figure 1A**). Old individuals display several visually apparent aging phenotypes, including spine curvature, craniofacial alterations, as well as melanocytotic tailfins in males (**Figure 1B**). The brain morphology of the turquoise killifish resembles that of a typical teleost (**Figure 1C**) and has been extensively described elsewhere[45]. The turquoise killifish genome contains two paralogs of the human amyloid precursor protein (APP) which encode the amyloid beta (Aβ) sequence, *appa* and *appb* (coding sequences provided in **Table S1**). Both paralogs show a highly conserved $A\beta_{1-42}$ sequence from human to killifish, as well as conserved beta- and gamma-secretase cleavage sites (**Figure 1D**). Alphafold3 predicts similar 3D architecture for killifish (*appa* derived) and human (*APP* derived) $A\beta_{1-42}$ multimers (**Figure S1A-D**). This becomes evident by the superposition of the C-terminal regions of the isolated monomers (**Figure S1E**). These findings suggest that the high aggregation propensity of $A\beta_{1-42}$ is likely conserved between killifish and humans. To investigate whether Aβ is detectable in the aged turquoise killifish brain, we performed immunohistochemistry using two Aβ-targeting antibodies. Considering that the available antibodies are not specifically raised against the killifish Aβ peptide, together with the known risks of misinterpretation of non-specific signals in the aged brain[46,47], we first addressed the binding specificity of the antibodies. To that end, we used the 4G8 antibody, targeting the $A\beta_{17-24}$ epitope which is fully conserved between humans and killifish, and can bind full-length APP and various APP-derivatives including Aβ. Additionally, we used the pE11 antibody, which targets N-terminally truncated and pyroglutamated Aβ, through recognition of the N-terminal pyroglutamate group and the first six amino acids after truncation ($A\beta_{pE11-16}$) (**Figure 1D**). While 4G8 broadly marks full-

121 length APP and its derivatives, pE11 specifically targets the post-translationally modified Aβ ($A\beta_{pE11}$),
122 enabling the tracking of cleaved and toxic Aβ rather than its precursors. We focused on detecting $A\beta_{pE11}$,
123 not $A\beta_{pE3}$, as the pE11 target epitope is conserved between humans and killifish. Even though the 4G8
124 and pE11 antibodies bind different epitopes of the $A\beta_{pE11}$ peptide, we found a strong co-localization
125 between 4G8 and pE11 signal throughout the anterior rhombencephalon (AR) of aged (6-month-old)
126 killifish (**Figure 1E**). To mitigate the possibility that both antibodies bind the same structure in an
127 epitope-independent manner, we blocked the epitopes by incubating antibodies with synthetic $A\beta_{pE11-42}$
128 peptide prior to the immunohistochemical staining. While incubation with albumin did not impact the
129 staining pattern of pE11 or 4G8, the signal of both antibodies was almost completely abolished by the
130 pre-incubation with $A\beta_{pE11-42}$ peptide, indicating that both antibodies bind to their targets in the killifish
131 brain through their epitope binding domains (**Figure S2A, B**). Taken together, we conclude that the aged
132 turquoise killifish brain contains APP-derivatives, including pyroglutamated Aβ.
133
134 **Turquoise killifish develop age-related brain inflammation while expressing key players of Aβ**
135 **biogenesis**
136 To investigate the age-dependent expression levels of *appa* and *appb*, as well as other key players of Aβ
137 biogenesis, we performed whole brain RNA-sequencing on six young (6-week-old) and six aged (6-
138 month-old) female turquoise killifish (**Table S2**). Interestingly, genes downregulated with age indicate a
139 strong decline in cellular proliferation (e.g. *mki67*), consistent with the reported loss of neurogenic
140 potential[24,34,35] (**Figure S3A, B**). Genes upregulated with age (e.g., *stat1*, *irf9*, *rsad2*, *cmpk2*) suggest a
141 strong age-related induction of inflammation (**Figure S3C**), in agreement with previous findings[24,28,35,36].
142 To validate a potential age-related inflammatory state in the turquoise killifish brain, we tested markers of
143 brain inflammation in the hypothalamus and optic tectum through immunohistochemistry by targeting
144 Lymphocyte Cytosolic Protein 1 (LCP1), a pan-leukocyte marker employed to visualize microglia in the
145 zebrafish and killifish brain[24,35,48] (**Figure S3D, E**). As LCP1 is an actin-binding protein, the staining
146 pattern visualizes cytoskeletal architecture of brain leukocytes (**Figure S3F).** We found a strong age-

147 related increase in the surface area covered by LCP1, which validates the age-related inflammatory state
148 suggested by the transcriptomics data (**Figure S3G)**. Next, to adress whether key players in Aβ
149 biogenesis are actively transcribed in the killifish brain and would support a potential role for Aβ during
150 killifish brain aging, we plotted their expression in young and aged brains (**Figure S3H**). These key
151 players include amyloid precursor proteins *appa*, *appb*, the APP family members *appl1*, *appl2*, the
152 glutaminyl cyclase *qpctl* which pyroglutamates Aβ, the beta-secretase *bace1* and the family member
153 *bace2* as well as the gamma-secretase subunits *psen1*, *psen2*, *ncstn* and *aph1b*. While all factors showed
154 consistent expression in the turquoise killifish brain, no age-related changes were observed at the mRNA
155 level. In summary, the aging killifish brain becomes subjected to a robust inflammatory state and
156 expresses transcripts encoding key players of Aβ biogenesis.
157

158 **$A\beta_{pE11}$ accumulates across the rostro-caudal axis of the killifish brain**

159 Next, we investigated whether the 4G8 and pE11 signals (**Figure 1D, E**) show any age-related changes.
160 In the anterior rhombencephalon (AR) of young 6-week-old fish, 4G8 signal is already detectable and
161 covers a similar percentage of the tissue area as seen in their aged 6-month-old counterparts (**Figure 2A-**
162 **C**), which may reflect the binding of 4G8 to full-length APP. In contrast, the young AR seems largely
163 devoid of any pE11 signal, while pE11 signal was robustly present in the aged AR (**Figure 2D-F**). These
164 findings suggest that while full-length APP and its derivatives might be present in the brain throughout
165 killifish lifespan, $A\beta_{pE11}$ accumulates only at a later age. To explore the full spatiotemporal extent of the
166 accumulation of pyroglutamated Aβ, we characterized the pE11 signal in seven different brain regions
167 along the rostro-caudal axis, at four different ages (**Figure 2G**, **Figures S4-8**). While the pE11 signal
168 remained nearly undetectable until three months of age, the pE11 covered surface area peaked at six
169 months, which was consistent in all investigated brain regions. At nine months of age, the pE11 covered
170 surface area showed a decreasing trend when compared to the six-month timepoint, which was validated
171 in an independent cohort (**Figure S9**). The decline in pE11 covered surface area between 6- and 9-months
172 of age suggests an increase in clearance, or a reduced production of $A\beta_{pE11}$. Alternatively, the reduction of

173 pE11 between 6- and 9-months could be due to the death of pE11^{+} cells, and/or due to the selective
174 disappearance of animals with high $A\beta_{pE11}$ levels. Taken together, these results indicate that $A\beta_{pE11}$
175 accumulates spontaneously across the rostro-caudal axis between 3- and 6-months of age in the brain of
176 the turquoise killifish.
177
178 **Amyloid beta predominantly localizes intraneuronally and colocalizes with TUNEL**
179 In the human AD etiology, Aβ is typically known to localize in extracellular beta-sheet aggregates known
180 as Aβ plaques but has also been described to localize intraneuronally[49–54]. To assess Aβ localization in the
181 killifish brain, we first investigated the occurrence of extracellular plaques using the 4G8 and pE11
182 antibodies. Through an immunohistochemical approach using these antibodies, we could not identify any
183 large extracellular signals which would be indicative of the formation of extracellular amyloid plaques.
184 Instead, we found that 4G8 and pE11 signal mainly localized around nuclei, suggesting a predominantly
185 intracellular localization (**Figure 1E**, **Figure S4-8**). To investigate the potential intraneuronal localization
186 of $A\beta_{pE11}$ in the aged killifish brain, we co-labeled pE11 together with an antibody targeting neuronal
187 nuclei (NeuN) and neuronal cytoplasmic marker acetylated tubulin (acTub). Indeed, pE11 localized
188 directly around NeuN^{+} nuclei (**Figure S10A**), indicating that $A\beta_{pE11}$ predominantly localizes
189 intraneuronally. To address whether the intraneuronal localization of pyroglutamated Aβ is unique to the
190 killifish or whether its localization is evolutionary conserved and also present in aged human brains, we
191 performed pE11 staining on the brains of normal non-pathological (>80 years old) and AD diagnosed
192 individuals (**Figure S10B, Figure S11, S12**). Strikingly, we detected intraneuronal pE11 signal in both
193 the cortex and the hippocampus of normal aged human brains, as well as in the brains of Alzheimer's
194 patients. In addition, we detected pE11 signal in extracellular plaques of the Alzheimer's disease brains,
195 which is in line with previous reports[55]. These findings indicate that pyroglutamated Aβ is not limited to a
196 specific human pathology, but instead is broadly present the in aged vertebrate brain in an intraneuronal
197 fashion. Pyroglutamated Aβ has been shown to be exceedingly neurotoxic[43]. Therefore, to investigate
198 whether pE11^{+} cells show signs of DNA double stranded breaks typically indicative of programmed cell

199 death, we adopted TUNEL staining. TUNEL$^+$ cells were nearly undetectable in young killifish brains but
200 were clearly detectable in aged brains (**Figure S13**, **S14A**). Importantly, in aged brains TUNEL signal
201 colocalized with pE11 signal (**Figure S14B**), which might suggest that spontaneous accumulation of
202 $A\beta_{pE11}$ could negatively affect neuronal survival in aged killifish. Indeed, TUNEL$^+$/NeuN$^+$ neurons were
203 detectable throughout the aging killifish rhombencephalon (**Figure S15**), which agrees with previous
204 findings indicating that the aging killifish brain is subjected to substantial neuronal degeneration[29,37–39].
205

206 **APP-derivatives aggregate in an age-related manner**

207 The aging killifish brain is characterized by substantial protein aggregation[28–33]. To determine whether
208 this includes Aβ-associated beta-sheet aggregation, we conducted a thioflavin-T assay. This assay detects
209 changes in the fluorescent emission profile of thioflavin-T upon its incorporation into beta-sheet
210 aggregates[56]. Aged brain lysates yielded higher thioflavin-T signal compared to their younger
211 counterparts, indicating an age-dependent increase in beta-sheets protein aggregates (**Figure S16**). To
212 directly test whether Aβ precursor protein derivatives show signs of age-related aggregation, we
213 performed a filter retardation assay[57]. In short, protein lysates derived from killifish brains of several ages
214 were applied to a filter, which retains protein aggregates of a specific size determined by the pore size of
215 the filter. Next, we stained the filter-bound aggregated protein with either the 4G8 or the pE11 antibody.
216 We found that while 4G8 signal was enriched in an age-dependent manner (**Figure S17A, B**), this was
217 not the case for the detected pE11 signal (**Figure S17C, D**). Corroborating the potential age-dependent
218 aggregation of 4G8$^+$/pE11$^-$ peptides, we detected an age-dependent increase in intracellular 4G8$^+$/pE11$^-$
219 puncta in the killifish brain (**Figure S18**), which may reflect intracellular aggregation of APP derivatives.
220 Indeed, 4G8$^+$ puncta showed a partial overlap with the Aggresome dye, which was previously employed
221 to visualize intracellular protein aggregation in the killifish brain[30] (**Figure S19**). The aged human brain
222 might display a similar discrepancy between 4G8 and pE11 signals, as the 4G8 signal showed a
223 granulated pattern in contrast to the pE11 staining (**Figure S20)**. Taken together, our results indicate that

224 APP-derivatives, but not necessarily $A\beta_{pE11}$, become increasingly aggregated with age in the brain of the
225 turquoise killifish.
226
227 **CRISPR/Cas9 mediated knock-out of *appa* results in reduction of APP-derivatives**
228 Given the age-dependent accumulation of Aβ, we speculated that Aβ might contribute to the aging
229 phenotypes of the killifish brain. To test this hypothesis, as well as to investigate whether amyloid
230 precursor protein can be targeted to reduce vertebrate brain aging phenotypes, we generated an *appa*
231 mutant line using CRISPR/Cas9. Using two guide RNAs targeting the second exon of the *appa* gene, we
232 introduced a 16bp deletion leading to a frameshift (**Figure 3A**). The induced frameshift did not lead to a
233 premature stop-codon but led to a randomized amino acid coding sequence, which prevented the
234 translation of *appa* derived Aβ peptide. In addition to *appa*, we also targeted its homolog, *appb*, for
235 knock-out. While successfully inserting mutations in the *appb* gene, founders could not be raised to
236 adulthood and were therefore excluded from analysis. The loss of *appb* mutant carriers might indicate a
237 role for *appb* in killifish development, which is in line with the described role for *appb* during early
238 embryonic development in the zebrafish[58]. To investigate whether *appb* acts redundantly to counteract the
239 lack of *appa*-derived APP, we performed a Western blot using the 22C11 antibody targeting the full-
240 length APP. 22C11 should target both wild-type APPA and APPB, as the epitope targeted by 22C11 is
241 highly conserved in both homologs (16/16 amino acids) and might also detect killifish APLP2 (12/16).
242 APLP1 is less conserved (9/16). We observed a significant reduction (>50%) of APP levels in the killifish
243 *appa* mutant brain lysates, indicating that the still functional *appb* could not compensate in full for the
244 loss of *appa* derived APP (**Figure 3B**, **C**). At 6-months of age, the reduced levels of APP led to a
245 reduction in APP-derivatives, including $A\beta_{pE11}$, indicated by the observed reduction in 4G8 and pE11
246 signal intensity as well as a reduction in the surface area covered (**Figure S21**, **Figure 3D**, **E**). The
247 reduced immunoreactivity for both antibodies in the *appa* mutants further supports their binding
248 specificity to peptides derived from the gene encoding for amyloid precursor protein a. Residual antibody
249 immunoreactivity likely stemmed from *appb* derived Aβ. Taken together, we have produced an *appa*

250 knock-out model which shows reduced levels of APP and its derivatives, including pyroglutamated
251 amyloid beta.
252
253 **Brain aging is mitigated through *appa* knock-out**
254 To investigate the effects of the knock-out of *appa* in an unbiased manner, we performed liquid
255 chromatography mass spectrometry (LC-MS) on whole brain lysates (**Table S3**). We used three males
256 and three females from both *appa* mutants, as well their wild-type siblings, for each of the two age groups
257 (6- and 7.5-month-old). The time-point of 7.5 months was chosen as it corresponds to the median lifespan
258 of fish from the ZMZ1001 strain (**Figure 1A**), at which behavioral changes become apparent[39,41]. At both
259 timepoints, *appa* derived peptides were undetectable in the *appa* mutants, while *appb* derived peptides
260 (APPB) showed no significant changes (**Figure 3F-I**). At 6-months of age, the *appa* mutants displayed an
261 upregulation of proteins involved in mitochondria (e.g. DHRS12, SLC25A3, NDUFV1), translation (e.g.
262 RPS7, RPL27, RPS13), and DNAJ-chaperones (e.g. DNAJC5AA, DNAJA1L, DNAJB3, DNAJA3A), as
263 well as a downregulation of amyloidosis associated factors Apolipoprotein A1 (APOA1) and beta-
264 synuclein (SNCB) (**Figure 3F**, **G**). Compared to same-aged wild-type siblings, 7.5-month-old *appa*
265 mutants showed an upregulation of keratins (e.g. KRT4, KRT5, KRT18) and a downregulation of
266 proteins involved in the lysosome and proteasome, as well as proteins involved in inflammation related
267 ontologies, such as the defense response (e.g. C4B, TGFB1), and the JAK-STAT cascade (e.g. STAT1A).
268 In addition, we observed downregulation of proteins involved in necroptosis (e.g. MLKL, XIAP) which is
269 suggestive of a reduction in programmed cell death (**Figure 3H**, **I**). To validate the potential mitigation of
270 age-related cell death in the *appa* mutants, we performed TUNEL staining in tissue sections of the
271 hypothalamus superior lobe and anterior rhombencephalon. While TUNEL$^+$ cells were consistently
272 present in brains of wild-type sibling, *appa* mutant brains contained a lower TUNEL$^+$ covered surface
273 area in both investigated regions at as early as 6-months of age (**Figure 3J-L**). In addition, staining for
274 (pro)caspase3, which marks (pre-)apoptotic cells[59], showed a similar decrease in 6-months-old *appa*
275 mutants (**Figure S22**). To validate the potential mitigation of age-related inflammation, we performed an

276 immunohistochemical staining using an antibody targeting Lymphocyte Cytosolic Protein 1 (LCP1) as
277 previously described (**Figure S3D-F**). The 6-months-old *appa* mutant brain displayed a significant
278 reduction of LCP1 covered surface area in the hypothalamus superior lobe, and a declining trend in the
279 anterior rhombencephalon (**Figure 3M-O**). Together, LC-MS and histology show that the knock-out of
280 *appa* mitigates spontaneous cell death and inflammation in the aging turquoise killifish brain. To
281 determine whether the beneficial effects of *appa* knock-out are restricted to inflammation and cell death,
282 or whether they represent a broader mitigation of brain aging, we investigated whether we could detect a
283 proteome-wide shift towards a younger proteome in the *appa* mutants compared to their wild-type
284 siblings. To that end, protein group abundances were compared between young (6-week-old) and aged (6-
285 month-old) brains, as well as between *appa* mutant and wild-type sibling brains at two different ages (6
286 and 7.5 months). Subsequently, the log2 fold-change (log2FC) values from both the young-versus-old and
287 appa mutant-versus-wild-type comparisons were plotted against one another. In 6-month-old *appa*
288 mutants, the differentially abundant proteins did not correlate with age-related changes in protein level
289 (**Figure 3P**). However, in 7.5-month-old *appa* mutants, we observed a highly significant negative
290 correlation (slope = -0.265, p = 2.31e-13) indicating that proteins upregulated with age were
291 downregulated in the mutants, and *vice versa* (**Figure 3Q**). Proteins upregulated with age but
292 downregulated in the *appa* mutants included proteins implicated in neurodegenerative diseases (e.g.
293 APOEB, PFN1, LGALS9) and inflammation (e.g. IFI44L, C4B, CMPK2), while proteins downregulated
294 with age and upregulated in the *appa* mutants included extracellular matrix components (e.g. COL1A2,
295 KRT5) as well as proteins involved in neuronal function (e.g. GRM8, PCDH2AC, PPFIA2). These
296 findings indicate that *appa* knock-out mitigated brain aging in a proteome-wide manner, extending
297 beyond the reduction of inflammation and cell death.
298
299 **Knock-out of *appa* mitigates age-related learning decline**
300 Turquoise killifish display a spontaneously occurring decline in learning capacity with age, a *bona fide*
301 measure of age-related cognitive decline[39,41]. To investigate whether APP/Aβ contributes to non-

302 pathological age-dependent learning deficiency, we developed an active avoidance test based on previous
303 literature[39,60,61]. In short, fish (28 *appa* mutants and 30 wild-type siblings) were individually tested by
304 placing them in an arena consisting of two circular compartments, connected through a narrow opening
305 (**Figure 4A**). After a 15-minute acclimatization period, fish were subjected to 40 consecutive cycles,
306 where a conditionate stimulus (light), was coupled with a non-conditioned stimulus (air bubbles). Each
307 one-minute cycle corresponded to 30 seconds of light exposure, with the latter 15 seconds combined with
308 exposure to air bubbles, followed by a rest phase of 30 seconds. Untrained fish showed a preference to
309 remain in the light, with 84% of the fish staying within the light during the first cycle of the experiment
310 (**Figure 4B**). Due to the pairing of the light with an adverse non-conditioned stimulus (air bubbles) across
311 the 40 cycles, the fish learn to avoid air bubbles once cued with light. Indeed, even 7.5-month-old wild-
312 type fish (n = 30) become increasingly proficient at actively avoiding the light with 16% (first cycle) to
313 46% (last cycle) of the fish escaping the bubbles (**Figure 4B**, **Figure S23**, **Table S4**). However, the 7.5-
314 month-old *appa* mutants (n = 28) outperform their age-matched wild-type siblings and show an increased
315 rate of successful escapes after the 6th cycle onwards, while reaching an average escape rate of 55%
316 during the last cycle (**Figure 4B**, **Figure S23**). Comparing the total amount of successes, as well as their
317 top scores, defined as the maximum number of successes in a 10-cycle window, show higher (yet non
318 statistically significant) learning performance in the *appa* -/- mutants (p = 0.073 and p = 0.265,
319 respectively) (**Figure 4C**, **D**). Significant improvements in the *appa* -/- mutants were observed when
320 comparing the speed at which their top scores were reached (**Figure 4E**) and when considering both top
321 scores and the speed (i.e. the number of the learning cycle) at which the top score was reached
322 simultaneously (**Figure 4F**). To gain insight into the biological significance of the learning improvements
323 observed in the *appa* -/- mutants at 7.5-months of age, we performed the active avoidance test on an
324 independent cohort of young killifish (6-week-old, n = 16) (**Figure S24**). While young fish show a higher
325 escape rate in the first 5 cycles of the experiment compared to all other non-young counterparts, the 7.5-
326 month-old mutants performed not only better than age-matched controls, but similar to young fish for the

327 remaining cycles. These results suggest that knock-out of *appa* can almost completely rescue the age-
328 related learning deficit observed in turquoise killifish.
329 Newly learned behaviors (e.g. the negative association with red light) are encoded within a neuronal
330 network which, upon activation, expresses the immediate response factor c-Fos[62,63]. To address whether
331 the active avoidance test we employed led to the activation of such network, and whether the *appa*
332 mutants show increased network activity compared to their wild-type siblings, we used Hybridization
333 Chain Reaction (HCR) *in situ* mRNA detection. We used HCR to visualize *fos* transcripts in brains
334 isolated immediately after the 40th cycle of the active avoidance task (**Figure 4G-J**). We specifically
335 quantified the percentage surface area covered by *fos* transcripts in the medial zone of the telencephalon
336 (**Figure 4K**), considering that this region has been previous implicated in learning performance of other
337 fish species[64]. We found that the *appa* mutants that underwent the active avoidance test showed higher
338 *fos* levels in the medial zone when compared to untested fish, as well as their wild-type siblings that did
339 undergo the active avoidance test (**Figure 4L**). From these results, we conclude that the knock-out of
340 *appa* rescued an age-induced learning deficit, which is associated with enhanced neuronal activity in the
341 telencephalon.
342
343
344
345
346
347
348
349
350
351
352

353 **Discussion**

354

355 In this study, we asked whether the detrimental effect of Aβ on the brain is limited to neurodegenerative
356 diseases, or whether Aβ also impacts normal, non-pathological brain aging. Although Aβ has been shown
357 to accumulate during normal aging[65], convincing experimental proof of its causal effect remained absent.
358 An important clue suggesting a potential causal effect of Aβ in the normal aging brain was provided by a
359 previous study describing the cognitive fitness of aged human carriers of the Islandic APP variant
360 (A673T). The A673T APP mutation leads to a reduction in β-Secretase 1 (BACE1)-mediated Aβ
361 production[66], which not only correlated with a reduced risk to develop Alzheimer's disease (AD), but also
362 with increased cognitive fitness in normal aging individuals[67]. Here, we provide the first experimental
363 evidence showing that lowering APP levels in spontaneously aging vertebrates can reduce brain aging
364 phenotypes and mitigate age-related cognitive decline.

365

366 To investigate the effect of Aβ during normal brain aging, we have employed the turquoise killifish.
367 These annual teleosts evolved a compressed lifespan due to the relaxed purifying selection of deleterious
368 mutations acting in late life[68]. Therefore, the turquoise killifish genome carries an exceptionally high
369 mutation load, which likely contributes to the polygenic basis of their robust aging phenotypes and
370 compressed lifespan. Due to their short lifespan, turquoise killifish represent an ideal model for functional
371 studies investigating vertebrate aging. In this study, we recapitulate previously reported brain aging
372 phenotypes of the turquoise killifish, including the aggregation of protein, inflammation, and cellular
373 degeneration. Furthermore, we describe an additional brain aging phenotype, the intraneuronal
374 accumulation of $A\beta_{pE11}$. Notably, we found that intraneuronal $A\beta_{pE11}$ not only characterizes the aging
375 brain of the killifish but is also present in aged, non-diseased human brains. Intraneuronal $A\beta_{pE11}$ had
376 previously been associated with Alzheimer's disease[69] but, to the best of our knowledge, remained largely
377 unexplored in the context of normal brain aging. While $A\beta_{pE3}$ is expressed and studied in AD mouse
378 models (e.g. 5xFAD)[70], no animal data were available to date for the endogenous expression of $A\beta_{pE11}$.

379 Our findings showing spontaneous intraneuronal $A\beta_{pE11}$ accumulation during aging in killifish reveal a
380 novel conserved association of Aβ in the context of natural brain aging. Several mechanisms could
381 explain intraneuronal $A\beta_{pE11}$ accumulation during aging, including an age-dependent increase in APP
382 endocytosis[71] further processed in the *trans*-Golgi network[72,73,74], or a decline in Aβ clearance efficiency.
383
384 Even though we found no evidence of age-related extracellular amyloid plaques in aged killifish brains,
385 we detected intracellular aggregation of APP derivatives in the aging killifish brain. While $A\beta_{pE11}$ has
386 been reported to be highly aggregation prone[75], most $4G8^+$ puncta were negative for pE11. In addition, we
387 did not detect an increase in $pE11^+$ peptides using the filter retardation assay. It seems plausible that these
388 results could be the consequence of low abundance of pyroglutamated Aβ, leading to detection
389 limitations. Alternatively, Aβ aggregation might have occurred prior to the formation of $A\beta_{pE11}$, which is
390 supported by our finding that $4G8^+$ puncta arise before robust pE11 signal (6 weeks versus 6 months,
391 respectively). Hence, the early aggregation of full length Aβ might in principle delay the formation of
392 $A\beta_{pE11}$, supporting a model where Aβ aggregation might be protective, preventing the formation of toxic
393 Aβ derivatives[76].
394
395 To test the impact of Aβ during normal aging, we knocked out one the amyloid beta precursor protein
396 coding genes, *appa*. The results obtained through LC-MS suggested that *appa* knock-out mitigated
397 cellular death and inflammation in aged killifish brains, which we validated through a histological
398 approach. Furthermore, proteome-wide analysis indicated that the beneficial effects of *appa* knock-out are
399 not restricted to inflammation and cell death but encompass a much broader, proteome-wide mitigation of
400 brain aging. The beneficial effects of *appa* knock-out on brain aging in the turquoise killifish is in stark
401 contrast with the negative effects observed in APP knock-out mice, which are viable but have altered
402 neurogenesis and smaller brains[77]. Aged APP knock-out mice display increased reactive gliosis in the
403 neocortex and hippocampus and show reduced locomotor activity[78], as well as reduced memory
404 retention[79]. It has been suggested that both excessive amounts of Aβ, as well as complete depletion of Aβ,

405 has negative effects on brain functionality[80]. As teleosts, turquoise killifish have been subjected to a
406 whole genome duplication[81] and hence, contain two APP paralogues. Therefore, while knockout of APP
407 in mice resulted in a complete depletion of Aβ, knock-out of *appa* in killifish left the fish with *appb*,
408 which might have yielded a concentration of Aβ high enough to allow typical brain development and
409 function, but low enough to evade Aβ-mediated exacerbation of brain aging phenotypes.
410
411 While decades of research have focused on elucidating the effect of Aβ during Alzheimer's disease, the
412 effects of Aβ accumulation during normal aging remained largely unexplored. Here, we show that
413 amyloid beta precursor protein exacerbates brain aging in a short-lived teleost. These findings indicate
414 that the detrimental effects of Aβ are not limited to a specific human pathology, but instead broadly
415 impact vertebrate brain aging. Aβ-targeting strategies, originally intended to mitigate neurodegenerative
416 diseases, may therefore have broader potential as an anti-aging approach to preserve cognitive health
417 throughout life.
418

419 **Methods**

420

421 *Fish husbandry and maintenance*

422 The turquoise killifish (ZMZ1001 strain) were housed in individual 2.8L tanks equipped with baffles, fry
423 mesh and lids glass capillaries (Aquaneering, USA) connected to a system with circulating water. Fish
424 received 12 h of light and 12 h of darkness per day. Water temperature was set to 28°C. Fish were fed
425 with brine shrimp nauplii (*Artemia salina*) and blood worm larvae (*Chironomus spp.*) twice a day during
426 the week and once a day during the weekend. Adult fish (6 weeks post hatching) were used for breeding
427 purposes. One male and up to three females were housed in 9.5L breeding tanks equipped with baffles,
428 fry mesh and lids glass capillaries (Aquaneering, USA). Fertilised eggs were regularly collected using
429 sand boxes and then stored in a petridish with coconut fiber at 24°C. Three weeks prior to hatching,
430 embryos were placed at 28°C. Furthermore, the husbandry and maintenance of the killifish used in this
431 study were performed as part of the standard operating procedure the Leibniz institute on Aging, which
432 was described in detail in a previous publication[82]. The experiments were carried out under permission of
433 the following animal experimental licenses: FLI-21-016 (young behavioral tests), FLI-23-029 (appa KO
434 versus wild-type behavioral tests), Par.11 J-003798 (Maintenance and Housing), FLI-22-203
435 (Genotyping), O-DV-23-27 (Organ harvest license).

436

437 *Protein alignment and Alphafold protein structure predictions*

438 To determine how similar protein sequences of APPA and APPB from turquoise killifish are to protein
439 sequences from humans (*H. sapiens*), mice (*M. musculus*) and zebrafish (*Danio rerio*), full-length peptide
440 sequences were aligned using UniPro UGENE (RRID:SCR_005579). Multiple protein sequences were
441 aligned with the MUSCLE default mode. The sequences of all protein variants from online database
442 Ensembl (https://www.ensembl.org/index.html). Structure predictions of $A\beta_{1-42}$ were performed using the
443 AlphaFold3 web server with default options[83]. For graphical representations the program ChimeraX[84] was
444 employed.

445

446 *Brain processing for cryo-sectioning*

447 Killifish were euthanized using rapid-chilling method. The whole head was first fixed in 4%
448 paraformaldehyde overnight at room temperature. The next day brain was isolated, washed in 4% sucrose
449 and incubated in 30% sucrose overnight at 4°C. On the last day, brain was transferred to an appropriate
450 Tissue-Tek cryomold, immersed in the Tissue-Tek O.C.T. Compound and transferred to the dry ice to
451 quickly freeze the tissue. Brains were stored at -80°C until the sectioning step. The tissue blocks were
452 sectioned to 10 µm thin sections using cryostat machine, while following standard protocol for cryo-
453 sectioning.

454

455 *Immunohistochemistry*

456 Thawed slides were first washed in PEMTx solution (80 mM 98.5+% PIPES (1,4-Piperazin-bis-
457 (ethansulfonacid), 5 mM EGTA, 1 mM $MgCl_2$, 0.2% Triton X-100 in milliQ water, pH 7,5) for 10 min, in
458 NH_4Cl-PEMTx (50 mM of NH_4Cl in PEMTx) for another 10 min, and then two more times in PEMTx.
459 The slides were transferred and incubated in Sodium Citrate Solution (10 mM 99% Trisodium Citrate
460 Dihydrate in RO H_2O, pH 6) for 15 min at 85°C in the waterbath. Once cooled down to the room
461 temperature, slides were washed two times for 10 min in PEMTx. The tissue was incubated in the
462 blocking solution (10% Fetal Bovine Serum, 1% DMSO in PEMTx) for 1 hour at room temperature in a
463 humidified chamber. Slides were later incubated with primary antibodies diluted in a blocking buffer at
464 4°C overnight in a humidified chamber. The following day, the slides were washed in PEMTx solution
465 five times for 20 min (on a shaker). The slides were incubated in the secondary antibody (1:500) and
466 DAPI (1:1000) diluted in a blocking buffer for 1 h at room temperature in a humidified chamber and in
467 the dark. The primary antibody Rabbit Anti-Abeta-pE11 was combined with the secondary antibody
468 Alexa Fluor® 647 Donkey anti-rabbit IgG (min. x-reactivity) antibody (BioLegend, USA, Cat# 406414,
469 RRID: AB_2563202). The Rabbit Anti-GFAP antibody was combined with the secondary antibody Alexa
470 Fluor 555 (Thermo Fisher Scientific, USA, Cat# A-21428, RRID: AB_2535849). The slides were washed

471 in PEMTx solution five times for 10 min, then two times for 7 min in PEM solution (80 mM 98.5+%
472 PIPES (1,4-Piperazin-bis-(ethansulfonacid), 5 mM EGTA, 1 mM $MgCl_2$ in miliQ H_2O) on the shaker and
473 in the dark. Slides were mounted in the ProLong Gold antifade reagent and stored at 4°C in the dark. The
474 slides were imaged using Zeiss Axio Scan.Z1 microscope with a Plan-Apochromat 20x/0.8 M27
475 objective, Axiocam 506m imaging device and 1x Camera Adapter. Imaging results were processed using
476 ZEN 3.5 (Blue Edition) ZEN Digital Imaging for Light Microscopy (RRID:SCR_013672) to select
477 images and Fiji (ImageJ2, RRID:SCR_002285) and Imaris (V10.2, 2024 June 26) to quantify positive
478 signal.
479
480 *Immunohistochemistry on human brain samples*
481 Human brain tissue samples of AD patients and aged-matched controls were obtained from the London
482 Neurogenerative Diseases Brain Bank, King's College London. For each individual, we used consecutive
483 tissue sections of 10 um thickness in order to visualize the precise localization of the staining for 4G8 and
484 pE11 in comparable areas.
485 Tissue sections deriving from 2 AD patients (BBN-ID: BBN_9888, 80, M, and BBN_002.34142, 77, M)
486 and 2 control individuals (BBN-ID: BBN002.36178, 86, M, and BBN_23398, 83, M) were
487 deparaffinized in two changes of xylene of 5 minutes each, followed by rehydration through a graded
488 series of ethanol (100%, 96%, 70%, 50%) for 5 minutes at each concentration and finally rinsed in
489 distilled water for 5 minutes. Acid antigen retrieval was performed using citrate buffer (10 mM, pH 6.0,
490 Tween 20, 0.05%) in a microwave oven. Tissue sections were submerged in the buffer and heated for 3
491 minutes at 95°C. After cooling to room temperature, the sections were washed in phosphate-buffered
492 saline (PBS, pH 7.4) three times for 5 minutes.
493 Endogenous peroxidase activity was quenched by incubating the sections in 3% hydrogen peroxide
494 (H_2O_2) in water for 10 minutes at room temperature, followed by two washes in PBS for 5 minutes each.
495 To reduce nonspecific binding, sections were incubated with normal serum (from the species of the
496 secondary antibody host) provided by the kit (ImmPRESS® HRP Goat Anti-Rabbit IgG Polymer Kit and

497 ImmPRESS® HRP Horse Anti-Mouse IgG Polymer Kit, MP-7451 and MP-7402, Vector Laboratories)
498 for 2 hours at room temperature.
499 Tissue sections were then incubated with the primary antibody (pE11, Synaptic Systems, 1:200 dilution
500 or 4G8, Biolegend, 1:500 dilution) diluted in PBS with 1% bovine serum albumin (BSA) and 0.1% Triton
501 X-100. Sections were incubated overnight at 4°C in a humidified chamber.
502 The day after, sections were rinsed in PBS three times for 5 minutes each. Sections were then incubated
503 with the appropriate HRP conjugated secondary antibody belonging to the kit for 1 hour at room
504 temperature. After washing with PBS (3 × 5 minutes), immunoreactivity was visualized using 3,3'-
505 diaminobenzidine (DAB) chromogen solution prepared according to the manufacturer's instructions
506 (DAB Peroxidase Substrate, SK-4100, Vector laboratories). Sections were incubated with DAB for 4-5
507 minutes, monitoring the color development under a light microscope. The colorimetric reaction was
508 stopped by rinsing the slides in distilled water.
509 For counterstaining, sections were immersed in hematoxylin for 3 minutes, rinsed in tap water, and
510 dehydrated through graded alcohols (50%, 70%, 96%, and 100%) followed by xylene. Finally, sections
511 were coverslipped with a permanent mounting medium (Permount mounting medium, SP15-100, Fisher
512 Chemical).
513 Additionally, we performed in parallel the same procedure on a sample from a control individual as
514 negative control, i.e. we treated the sections as described above, omitting only the addition of any primary
515 antibody to the solution prior to the overnight incubation.
516 Immunostained sections were then imaged using a light microscope (Nikon Eclipse600) equipped with a
517 DS-Fi3 color camera (Nikon, Tokyo, Japan) and a double LED light O-ring.
518
519 *PROTEOSTAT aggresome staining*
520 To detect intracellular protein aggregation, we used the PROTEOSTAT® Aggresome detection kit (ENZ-
521 51035, Enzo Life Sciences). In short, following the immunohistochemical detection of 4G8, slides were
522 incubated for 30 minutes in a dark humidified box with Aggresome staining solution (1:500). Next, slides

523 were washed three times in PBS, followed by mounting in prolong gold. Imaging was done using Ex/Em
524 wavelengths of 550 – 565-600nm, respectively.
525
526 *Used antibodies:*

Antibody	**Used for**	**Dilution**	**Ordering details**
Rabbit polyclonal purified Anti-Abeta-pE11	IHC	1:200	Synaptic Systems, AB_2619913
Mouse anti APP A4 clone 22C11	WB	1:5000	Millipore, MAB348
anti-mouse IgG HRP conjugate	WB	1:10000	Promega, W402B
Mouse anti-a-tubulin	WB	1:100000	Sigma, T6199
Anti-Acetylated Tubulin, Mouse Monoclonal (Clone 6- 11B- 1)	IHC	1:100	Sigma-Aldrich, T7451
Anti-β-Amyloid, 17-24 Antibody (4G8), mouse monoclonal	IHC	1:100	Biolegend, SIG-39200
Anti-LCP1, rabbit polyclonal	IHC	1:100	GeneTex, GTX124420
Anti-NeuN, mouse monoclonal (clone A60)	IHC	1:150	Sigma-Aldrich, MAB377
Anti-Caspase-3 (31A1067), mouse monoclonal	IHC	1:100	Novus, NB100-56708SS
Anti-rabbit Alexa555 (IgG, H+L)	IHC	1:500	Invitrogen, A21428
Anti-rabbit Alexa647 (IgG, H+L)	IHC	1:500	Invitrogen, A27040
Anti-mouse Alexa555 (IgG, H+L)	IHC	1:500	Invitrogen, AB_2535844
Anti-mouse Alexa647 (IgG, H+L)	IHC	1:500	Invitrogen, A21235
Anti-rabbit-HRP	FRA	1:5000	Dianova
Anti-mouse-HRP	FRA	1:2000	Sigma-Aldrich

527
528 *RNA sequencing*
529 Brain dissection was followed by RNA isolation using the TRIzol reagent (Life Technologies, Carlsbad,
530 CA, USA) according to the manufacturer's instructions. RNA integrity and concentration were measured
531 using Agilent 4200 TapeStation System in combination with RNA ScreenTape (Agilent Technologies,
532 Santa Clara, CA, US) ensuring high quality RNA (RNA Integrity Numbers > 8) for library preparation.
533 Libraries for Illumina next-generation sequencing technology[85] were prepared from 200 ng of total RNA

534 using NEBNext Ultra II Directional RNA Library Preparation Kit in combination with NEBNext Poly(A)
535 mRNA Magnetic Isolation Module and NEBNext Multiplex Oligos for Illumina (Unique Dual Index UMI
536 Adaptors RNA) following the manufacturer's instructions (New England Biolabs, Ipswich, MA, US).
537 Library quantification and quality assessment were performed using Agilent 4200 TapeStation System with
538 D5000 ScreenTape. Libraries were then pooled and sequenced on NovaSeq 6000 platform (Illumina, San
539 Diego, CA, US) using the SP 100 cycle v1.5 kit with a 51-cycle paired-end read configuration. A minimum
540 sequencing depth of 33.2 million reads per sample was achieved. Sequencing data were converted to
541 FASTQ format using bcl2fastq (v2.20.0.422).
542
543 *RNA sequencing data analysis*
544 Raw sequencing data (FASTQ files) were evaluated for quality using FastQC (v0.11.9). Adapter sequences,
545 poly-A sequence and low-quality bases were removed using cutadapt (v4.2). High-quality reads were
546 aligned to the reference genome (*Nothobranchius furzeri*, MPIA_NFZ_2.0) using STAR (2.7.6a) and PCR
547 duplicates were removed based on unique molecular identifiers by umi-tools (1.1.1, parameter: --chimeric-
548 pairs discard --unpaired-reads discard –paired). Gene-level quantification was performed using
549 featureCounts (v2.0.3, parameter: -s 2 -p -B --countReadPairs) based on annotated gene features (obtained
550 through personal communication with David Willemsen, corresponding to[86]. Differentially expressed genes
551 were obtained using the R package EdgeR[87] and gene ontologies were obtained using the online tool
552 DAVID[88].
553
554 *TUNEL staining*
555 To visualize apoptotic cells in the killifish brain, cryosections (fixed in 4% PFA, sectioned 10um thick)
556 were stained using the In Situ Cell Death Detection Kit, TMR rot (12156792910) from Roche. In short,
557 cryosections were air dried for 15 seconds, and washed in PBS + 0,2% Triton-X100 for 3 times 10
558 minutes. Three washes in PBS, of each 5 minutes, were followed by placing the slides in a humidified
559 box, and the brain sections of interest were encircled by a hydrophobic pen. Next, TUNEL staining

560 solution was added on top of the sections which were placed, inside of the humidified box, in a 37°C
561 incubator for 60 minutes. Afterwards, the slides were washed 3 times for 5 minutes in PBS and incubated
562 with PBS+ DAPI (1:000 dilution) for 20 minutes in the humidified box. Last, the slides were washed 3
563 times for 5 minutes with PBS and mounted using Prolong Gold. Imaging and quantification were
564 performed as described for immunohistochemistry, utilizing TUNELs excitation spectrum at 540nm and a
565 emission spectrum between 570-620nm.
566
567 *Western blot analysis*
568 Liquid frozen brains of killifish appa -/- and age matched controls of 6-months of age were lysed in
569 300µls 4xLämmli sample buffer (4 ml 20% SDS, 4 ml glycerol, 1ml ß-mercaptoethanol, 1 pinch
570 bromophenol blue, 1,25 ml 1M Tris pH 7,6) using a tissue homogenizer. After boiling for 10 min at 95°C
571 while shaking at 600 rpm, the samples were centrifuged 1 min at 11000 rpm. 20µls of the total lysate
572 were loaded on Schägger gels. After 60 mins transfer to nitrocellulose blotting membrane (0,1 µm,
573 Amersham™ Protran, product 10600005) at 400 mA, the membrane was boiled for 5 mins in 1 x PBS,
574 then incubated in 1 x PBS for 30 mins at room temperature before blocking with 0,2% Tropix I-Block
575 (Applied Biosystems) for 1 hr at room temperature on a rotating platform. The incubation in primary
576 antibody 22C11 (Mouse anti APP A4 clone 22C11, Millipore MAB348, 1:5000 in I-Block) was done
577 overnight at 4°C. After removal of the primary antibody, the membrane was washed 4 x 15 mins in I-
578 Block, followed by 1 hr incubation in a 1:10000 dilution of the secondary antibody (anti-mouse IgG HRP
579 conjugate, W402B, Promega) at room temperature. The membrane was washed 4 times 15 mins and 3
580 times 10 mins with 1 x PBS before detection of bound antibodies with ECL plus (Pierce ECL Plus
581 Western Blotting substrate, Thermo Scientific). After images were acquired using the LAS-4000 image
582 reader (Fujifilm Life Science), the membrane was washed 4 x 15min in PBST, blocked in 3%milk for 1hr
583 at room temperature and then incubated with the primary anti-a-tubulin antibody T6199 (Sigma) 1:100
584 000 in I-Block overnight at 4°C. After removal of the anti-a-tubulin antibody antibody, the membrane
585 was washed 4 x 15 min in I-Block, followed by 1 hr incubation in a 1:10000 dilution of the secondary

586 antibody (anti-mouse IgG HRP conjugate, W402B, Promega) at room temperature. The membrane was
587 washed 4 x 15 min and 3 x 10 min with 1 x PBS before detection of bound antibodies with ECL plus
588 (Pierce ECL Plus Western Blotting substrate, Thermo Scientific). Images of 22C11 and a-tubulin were
589 quantified with the software ImageJ. For each group biological triplicates were quantified.
590
591 *Thioflavin-T assay*
592 Whole brain protein lysates were produced using the same protocol as described to LC-MS. Black and
593 transparent bottom 96-well plate (Greiner 96 F-bottom, Thermo Fisher #165305) were used, as well as the
594 CLARIOstar Plus (BMG Labtech) plate reader. Thioflavin-T powder was bought from Sigma-Aldrich
595 (T3516). To produce the Thioflavin-T (ThT) working solution, 80mg of ThT-powder was added to 25mL
596 of dPBS (Gibco, [-] Cacl [-] MgCl) to make a 10mM stock. The solution was vortexed and incubated for
597 1 hour at room temperature. After the almost complete dissolvement of the ThT, 10mL of the ThT
598 solution was filtered through a 0.2µm filter using a syringe. Next, 200µl of the filtered ThT solution was
599 added to 1700µl of dPBS, to make the working solution of 50µM, and kept in the dark until further use.
600 Next, protein lysates (49µl of 1.325µg/µl) was added to the 96-well plate (F-bottom). Using a
601 multichannel pipet, 1µl of the ThT working solution (50µM) was added to the wells, and the plate was
602 entered in the plate reader directly. The following imaging settings were used: Microplate: Greiner 96 F-
603 bottom; Presets: CFP; Exitation: 430-20nm; Dichroic: auto 455nm; Emission: 480-20nm; Well scan:
604 none; Optic: Bottom optic; Settling time: 0.2; Flying mode: off; No. of kinetic windows: 1; No. of cycles:
605 10; No. of flashes: 50; Cycle time: 60; Shake: Before first cycle; double orbital, 100rpm, 10sec. Values
606 were recorded after 3 minutes and 30 seconds. Biological replicates were used in duplo, and averaged
607 values were plotted.
608
609 *Filter retardation assay*
610 Brain tissues were transferred to 2 mL Precellys tubes containing a mix of 1.4 mm and 2.8 mm ceramic
611 (zirconium oxide) beads, in 200 µL of BPS-PIS buffer. Two cycles of mechanical homogenization were

612 carried out at 6000 rpm for 30 seconds each, with a 30-second break on ice between each cycle, using the
613 Precellys 24 lysis and homogenizer (Bertin, France). Subsequently, the tubes were centrifuged at 3000
614 rpm for 5 min at 4°C. The resulting supernatant was carefully transferred to a new 1.5 mL low-binding
615 tube. An equal volume of 2X lysis buffer was added to the homogenate and sonicated (Bioruptor Plus,
616 Diagenode, Belgium) for 20 cycles (60 sec ON/30 sec OFF) at 4°C. The protein concentration in the
617 lysate was quantified using the Pierce™ BCA Protein Assay Kit (Thermo Fisher Scientific, Cat. no.
618 23227). For the filter retardation analysis, we adapted a previously published protocol[57]. In brief, 100 µg
619 of protein was loaded in duplicate onto a 0.2 µm cellulose acetate membrane (Cytiva, Cat. no. 10404180)
620 that had been pre-equilibrated in 1X TBS. The membrane was washed twice with a wash buffer (150 mM
621 NaCl and 10 mM Tris, pH 8.0), then blocked with 5% milk. This was followed by incubation with
622 primary antibodies: Rabbit-anti-pE11 (1:500, Synaptic Systems) or Mouse-anti-4G8 (1:1000,
623 BioLegend), overnight. Subsequent incubation with secondary antibodies was performed using anti-
624 rabbit-HRP (1:5000, Dianova) and anti-mouse-HRP (1:2000, Sigma-Aldrich) for 4 h. The images were
625 captured in Amersham imager 600, and quantification was performed using Fiji ImageJ software. Buffers:
626 BPS-PIS: 250 µL PBS; 5 µL Protease inhibitor cocktail; 25 µL PhosSTOP. Lysis Buffer (2X): 225 µL
627 PBS; 25 µL SDS (10%); 12.5 µL HEPES (2M). Tris-buffered saline (TBS) 10X, pH 8: 200 mM Tris
628 base; 1.5 M NaCl. Tris-buffered saline with Tween (TBS-T): 1X TBS; 0.1% Tween 20.
629
630 *CRISPR/Cas9 transgenesis*
631 CRISPR/Cas9 tool was used to edit the genome of the turquoise killifish. Guide RNA templates were
632 designed using an online program CHOPCHOP (https://chopchop.cbu.uib.no/). Exon 2 of *appa* was
633 targeted using two different gRNAs, and Exon 3 of *appb* was targeted using three different gRNAs.
634 Templates of ssDNA target-specific oligonucleotides were used for sgRNA synthesis. Used guide RNA's
635 (regions in bold indicate the complement sequence of the target):

***appa* sgRNA1**	TAATACGACTCACTATAGG**TCAACGTTCAGAGCGGCAAG**GTTTTAGAGCTAGAAATA GCA
***appa* sgRNA2**	TAATACGACTCACTATAGG**CAAGTGGGAGTCCGACCCCT**GTTTTAGAGCTAGAAATAGCA

***appb* sgRNA 1**	TAATACGACTCACTATAGG**AAACCCACCGAGTCATCCAAAG**GTTTTAGAGCTAGAAATAGCA
***appb* sgRNA 2**	TAATACGACTCACTATAGG**ACAGATCACGAATGTCGTAG**GTTTTAGAGCTAGAAATAGCA
***appb* sgRNA 3**	TAATACGACTCACTATAGG**CATTCGTGATCTGTAGCTCT**GTTTTAGAGCTAGAAATAGCA

636

637 The template ssDNA target-specific oligonucleotide to synthesise gRNA was designed by adding an
638 overlapping nucleotide sequence to the N-terminus and T7 promoter sequence to the C- terminus. The
639 PAM sequence (NGG) was removed from the sequence. Templates were synthesised and delivered by the
640 Integrated DNA Technologies (https://eu.idtdna.com/pages/products/custom-dna-rna/dna-oligos). The
641 sgRNAs were synthetised using the EnGen® sgRNA Synthesis Kit (New England BioLabs, USA,
642 #E3322V), according to their standardized protocol. The synthesised sgRNAs was cleaned up with the
643 Monarch® RNA Cleanup Kit (50µg, New England BioLabs, USA, #T2040L), following the instructions.
644 For CRISPR/Cas9 injections, concentration of sgRNA solution was adjusted to 300 ng/µL. The
645 CRISPR/Cas9 and gRNA reaction mix was prepared with EnGen® Spy Cas9 NLS (20 µM, New England
646 Biolags, USA), by mixing 1 µL of Cas9 NLS, 1 µL of each purified sgRNA (300 ng/µL), 2 µL Phenol
647 Red for visualisation and nuclease free water up to 10 µL (kept on ice). The needles were pulled from
648 glass capillaries 1.0 OD x 0.58 ID x 100 L mm using a micropipette puller machine with the program
649 previously established in the lab. One- or two-cell stage embryos were placed and fixed in the agarose
650 plate and injected with a small amount of reaction mix directly into the embryos one at a time. The
651 embryos were transferred to the clean methylene blue solution, checked daily and further handled as
652 previously described for embryo maintenance. To genotype CRISPR/Cas9 injected fish and their progeny,
653 first fish DNA had to isolated from 2-4 scales which were collected from the posterior part of the body of
654 sexually matured fish (minimum 5-6 weeks of age). The scales were transferred to 50 µL of SEL buffer
655 (1M KCl, 1M $MgCl_2$, 1M Tris pH 8,3, 10% Igepal, 10% Tween-20, 0,1% Gelatine in miliQ H_2O) and 1
656 µL of Proteinase K. The scales were incubated in the SEL isolation buffer and Proteinase K at 60°C for 1
657 h, 90°C for 15 min and 12°C until tubes were taken out of the machine. The isolated DNA was used as a
658 template for PCR amplification of the target region of interest. *Taq* 2X Master Mix was used for the PCR

659 reaction. PCR details. Forward primer: CCTCTCTTTCAGGTCCCCAC. Reverse primer:
660 TTTTCTGCTCTGCT TTTAGGC. Amplicon Length: 209 bp. CONDITIONS: **(1x)** 3:00 95.0C **(35x)**
661 0:45 95.0C 0:30 55.0C 0:45 72.0C **(1x)** 5:00 68.0 ∞ 10.0 PCR amplicons were purified using Sera-Mag
662 SpeedBead Carboxylate-Modified Magnetic Particles (Hydrophylic) magnetic beads. Purified DNA was
663 sent for Sanger sequencing to the Eurofins Genomics (https://eurofinsgenomics.eu/).
664
665 *Sample preparation for proteomics analysis*
666 Before lysis, lysis buffer (fc 4% SDS, 100 mM HEPES, pH 8.5, 50 mM DTT) was added to each samples.
667 Samples were then boiled at 95°C for 7 min and sonicated using a tweeter. Reduction was followed by
668 alkylation with 200 mM iodoacetamide (IAA, final concentration 15 mM) for 30 min at room temperature
669 in the dark. Samples were acidified with phosphoric acid (final concentration 2.5%), and seven times the
670 sample volume of S-trap binding buffer was added (100 mM TEAB, 90% methanol). Samples were bound
671 on 96-well S-trap micro plate (Protifi) and washed three times with binding buffer. Trypsin in 50 mM
672 TEAB pH 8.5 was added to the samples (1 µg per sample) and incubated for 1 h at 47°C. The samples were
673 eluted in three steps with 50 mM TEAB pH 8.5, elution buffer 1 (0.2% formic acid in water) and elution
674 buffer 2 (50% acetonitrile and 0.2% formic acid). The eluates were dried using a speed vacuum centrifuge
675 (Eppendorf Concentrator Plus, Eppendorf AG, Germany) and stored at -20° C. The samples were loaded
676 on Evotips (Evosep) according to the manufacturer's instructions. In short, Evotips were first washed with
677 Evosep buffer B (acetonitrile, 0.1% formic acid), conditioned with 100% isopropanol and equilibrated with
678 Evosep buffer A. Afterwards, the samples were loaded on the Evotips and washed with Evosep buffer A.
679 The loaded Evotips were topped up with buffer A and stored until the measurement.
680
681 *LC-MS Data independent analysis (DIA)*
682 Peptides were separated using the Evosep One system (Evosep, Odense, Denmark) equipped either with a
683 15 cm x 150 µm i.d. packed with a 3 µm Reprosil-Pur C18 bead column (Evosep Endurance, EV-1109,
684 PepSep, Marslev, Denmark) or with a a 15 cm x 150 µm i.d. packed with a 1.5 µm Reprosil-Pur C18 bead

685 column (Evosep Performance, EV-1137, PepSep, Marslev, Denmark) heated at 45°C with a butterfly sleeve
686 oven (Phoenix S&T, Philadelphia, USA). The samples were run with a pre-programmed proprietary Evosep
687 gradient of 44 min (30 samples per day) using water and 0.1% formic acid and solvent B acetonitrile and
688 0.1% formic acid as solvents. The LC was coupled to an Orbitrap Exploris 480 (Thermo Fisher Scientific,
689 Bremen, Germany) using PepSep Sprayers and a Proxeon nanospray source. The peptides were introduced
690 into the mass spectrometer via a PepSep Emitter 360-µm outer diameter × 20-µm inner diameter, heated at
691 300°C, and a spray voltage of 2 kV was applied. The injection capillary temperature was set at 300°C. The
692 radio frequency ion funnel was set to 30%. For DIA data acquisition with endurance column, full scan mass
693 spectrometry (MS) spectra with a mass range of 350–1650 m/z were acquired in profile mode in the
694 Orbitrap with a resolution of 120,000 FWHM. The default charge state was set to 2+, and the filling time
695 was set at a maximum of 60 ms with a limitation of 3 × 106 ions. DIA scans were acquired with 40 mass
696 window segments of differing widths across the MS1 mass range. Higher collisional dissociation
697 fragmentation (normalized collision energy 29%) was applied, and MS/MS spectra were acquired with a
698 resolution of 30,000 FWHM with a fixed first mass of 200 m/z after accumulation of 1 × 106 ions or after
699 filling time of 45 ms (whichever occurred first). Data were acquired in profile mode. For DIA data
700 acquisition for Performance column, full scan mass spectrometry (MS) spectra with a mass range of 350–
701 1650 m/z were acquired in profile mode in the Orbitrap with a resolution of 120,000 FWHM. The default
702 charge state was set to 2+, and the filling time was set at a maximum of 20 ms with a limitation of 3 × 106
703 ions. DIA scans were acquired with 45 mass window segments of differing widths across the MS1 mass
704 range. Higher collisional dissociation fragmentation (normalized collision energy 30%) was applied, and
705 MS/MS spectra were acquired with a resolution of 30,000 FWHM with a fixed first mass of 200 m/z after
706 accumulation of 1 × 106 ions or after filling time of 45 ms (whichever occurred first). For data acquisition
707 and processing of the raw data, Xcalibur 4.5 (Thermo) and Tune version 4.0 were used.
708
709 *Proteomic data processing*

710 DIA raw data were analysed using the directDIA pipeline in Spectronaut (v.17 and v.18, Biognosysis,
711 Switzerland). The data were searched against an in house species-specific database (*N.furzeri*, 59154
712 entries, Nfu_20150522, annotation nfurzeri_genebuild_v1.150922) with a list of common contaminants
713 appended (247 entries). The data were searched with the following variable modifications: oxidation (M)
714 and acetyl (protein N-term). A maximum of 2 missed cleavages for trypsin and 5 variable modifications
715 were allowed. The identifications were filtered to satisfy an FDR of 1% at the peptide and protein levels.
716 Relative quantification was performed in Spectronaut for each paired comparison using the replicate
717 samples from each condition. Precursors were percentile filtered at 0.2%. The data (candidate table) and
718 data reports (protein quantities) were then exported, and further data analyses and visualization were
719 performed with R studio using in-house pipelines and scripts. Differentially abundant proteins were defined
720 as having a q-value <0.
721
722 *Active avoidance test*
723 We assessed the decline in learning ability of treated fish using an active avoidance behavioral test which
724 was developed based on a test previously employed in killifish[39,41]. The setup consisted of two circular
725 compartments connected through a small opening. Fish were acclimatized for 15 minutes in water from
726 their home tank before testing began. A red light served as the conditioned stimulus, followed by air
727 bubbles as the negative stimulus. Fish learned to avoid the negative stimulus by crossing the small
728 opening into the opposite compartment when the red light appeared. The red light was presented for 30
729 seconds, with bubbles introduced after 15 seconds if the fish had not moved. Trials were counted as
730 'success' if the fish crossed the hurdle within 15 seconds of the red-light onset (before the introduction of
731 bubbles). The cycle of stimulus, bubbles, and rest repeated 40 times per fish. Each fish underwent the test
732 individually and was sacrificed immediately afterward. The entire test lasted one hour per animal. The
733 water temperature was kept stable between 26.5°C and 28.0°C using a standard aquarium heater, which
734 was important as varying temperatures could impact the performance of the fish.
735

736 *Hybridizing Chain Reaction*

737 Probe pair pools targeting *fos* and *neun* transcripts were generated and validated as previously
738 described[35,89]. The probe sequences can be found in **Table S5**. The selected probe pairs were ordered from
739 Integrated DNA Technologies, Inc. (IDT). The HCR protocol (HCRv3.0) was followed as previously
740 published[90] with adaptations for cryosections as described by Van Houcke et al. (2021)[24]. Cryosections of
741 10um thick were used. The amplification of the signal was done for *fos* transcripts with HCR Amplifier
742 B1, Alexa Fluor 647 and *neun* transcripts with HCR Amplifier B2, Alexa Fluor 546. Imaging was done
743 with the Zeiss Axio Scan.Z1 microscope with a Plan-Apochromat 20x/0.8 M27 objective, Axiocam 506m
744 imaging device and 1x Camera Adapter.

745

746

Acknowledgements

We are thankful to the Core Facility Proteomics, Imaging, Histology & Electron Microscopy, and Next Generation Sequencing at the FLI. We are thankful to the Animal fish Facility of the FLI, with a special mention of Johannes Wilfert, as well as Matthias Werres and Christina Paetzold from the fish facility of the MPI-AGE. We would like to thank the group of Lutgarde Arckens at K.U. Leuven (Belgium), and especially Caroline Zandecki, for the help with setting up the hybridizing chain reaction experiment. We are thankful to the group of Randal Halfmann (Stowers Institute) for the expert advice and help with the interpretation of the data, as well as Mario Baumgart for his help with importing the *appa* mutant line to the FLI. D.E.M. de Bakker was financed by a Rubicon scholarship (452021116) from the Dutch Research Council (NWO) as well as by a research grant from the "Balance of the Microverse" Excellence Cluster from the Friedrich Schiller University in Jena. We acknowledge the contribution of the London Neurogenerative Diseases Brain Bank (which is part of the Brains for Dementia Research network, jointly funded by Alzheimer's Research UK and the Alzheimer's Society) that provided us with the human-derived brain samples utilized in this study. This project was funded by the MPI-AGE and from the FLI in Jena. We would like to thank all the past and current members of the Valenzano lab at the MPI-AGE and at the FLI for their continuous input and support.

Data availability

The produced transcriptomic datasets will be made publicly available at the Gene Expression Omnibus from NCBI. Proteomics data will be made publicly available at MassIVE, which can be found following the links below. Proteomics data for Young (6 weeks) versus Old (6 months) *N. furzeri* brains:

http://massive.ucsd.edu/ProteoSAFe/status.jsp?task=650a5a2e981540359f34b145717d2f7b

Proteomics data for *N. furzeri appa* -/- versus *appa* +/+ brains:

http://massive.ucsd.edu/ProteoSAFe/status.jsp?task=e7c08aa99a7a427c8ec6eb2623a9e5ec

Declaration of interests

The authors declare no competing interests.

Author contributions

DdB planned the project, managed, designed, and executed most of the experiments including histology, behavioral analysis, and statistical and bioinformatical analysis, produced the figures, acquired funding, and wrote the manuscript. **MM** generation the appa KO line and histological analysis. Produced supplementary figures (S4-8). **KG** and **YR** performed the Filter Retardation Assay. **SB** performed histology on human samples. **FvB:** performed 22C11 Western Blot and critical contributed to the experimental design and interpretation. **BS** Critically contributed to the experimental design and interpretation. **LA** Assisted **DdB** with brain isolation and immunohistochemistry. **FSS** set up and performed HCR experiments. **OO** ran the AlphaFold model. **MB** supervised the transcriptomic data production and analysis. **EC** supervised the proteomic data production and analysis. **AA** shared resources and provided input on the manuscript. **IM** contributed to the manuscript draft. **AS** helped with project conceptualization and provided the pE11 antibody. **AC** aided with sample acquisition and critically contributed to the manuscript draft. **JK** supervised the biochemical analysis of protein aggregation and critically contributed to the manuscript draft. **DRV** Planned and supervised the project, wrote the manuscript, and acquired the funding.

Bibliography

1. Wyss-Coray, T. Ageing, neurodegeneration and brain rejuvenation. *Nature* vol. 539 Preprint at https://doi.org/10.1038/nature20411 (2016).
2. Pluvinage, J. V. & Wyss-Coray, T. Systemic factors as mediators of brain homeostasis, ageing and neurodegeneration. *Nat Rev Neurosci* **21**, 93–102 (2020).
3. de Bakker, D. E. M. & Valenzano, D. R. Turquoise killifish: A natural model of age-dependent brain degeneration. *Ageing Res Rev* **90**, (2023).
4. Murphy, M. P. & Levine, H. Alzheimer's Disease and the β-Amyloid Peptide. *J Alzheimers Dis* **19**, 311 (2010).
5. Sehar, U., Rawat, P., Reddy, A. P., Kopel, J. & Reddy, P. H. Amyloid Beta in Aging and Alzheimer's Disease. *Int J Mol Sci* **23**, (2022).
6. Alvarez, J., Alvarez-Illera, P., Santo-Domingo, J., Fonteriz, R. I. & Montero, M. Modeling Alzheimer's Disease in Caenorhabditis elegans. *Biomedicines* **10**, (2022).
7. Gallrein, C. *et al.* Novel amyloid-beta pathology C. elegans model reveals distinct neurons as seeds of pathogenicity. *Prog Neurobiol* **198**, (2021).
8. O'Keefe, L. & Denton, D. Using Drosophila Models of Amyloid Toxicity to Study Autophagy in the Pathogenesis of Alzheimer's Disease. *BioMed Research International* vol. 2018 Preprint at https://doi.org/10.1155/2018/5195416 (2018).
9. Iijima, K. *et al.* Dissecting the pathological effects of human Aβ40 and Aβ42 in Drosophila: A potential model for Alzheimer's disease. *Proc Natl Acad Sci U S A* **101**, 6623–6628 (2004).
10. Forner, S. *et al.* Systematic phenotyping and characterization of the 5xFAD mouse model of Alzheimer's disease. *Scientific Data 2021 8:1* **8**, 1–16 (2021).
11. Yokoyama, M., Kobayashi, H., Tatsumi, L. & Tomita, T. Mouse Models of Alzheimer's Disease. *Front Mol Neurosci* **15**, (2022).
12. Poon, C. H., Wang, Y., Fung, M. L., Zhang, C. & Lim, L. W. Rodent Models of Amyloid-Beta Feature of Alzheimer's Disease: Development and Potential Treatment Implications. *Aging Dis* **11**, 1235 (2020).
13. Zhang, Y., Chen, H., Li, R., Sterling, K. & Song, W. Amyloid β-based therapy for Alzheimer's disease: challenges, successes and future. *Signal Transduction and Targeted Therapy 2023 8:1* **8**, 1–26 (2023).
14. van Dyck, C. H. *et al.* Lecanemab in Early Alzheimer's Disease. *N Engl J Med* (2022) doi:10.1056/NEJMOA2212948/SUPPL_FILE/NEJMOA2212948_APPENDIX.PDF.
15. Cummings, J. Anti-Amyloid Monoclonal Antibodies are Transformative Treatments that Redefine Alzheimer's Disease Therapeutics. *Drugs* **83**, 569–576 (2023).
16. Budd Haeberlein, S. *et al.* Two Randomized Phase 3 Studies of Aducanumab in Early Alzheimer's Disease. *Journal of Prevention of Alzheimer's Disease* **9**, 197–210 (2022).
17. Swanson, C. J. *et al.* A randomized, double-blind, phase 2b proof-of-concept clinical trial in early Alzheimer's disease with lecanemab, an anti-Aβ protofibril antibody. *Alzheimers Res Ther* **13**, (2021).
18. Sevigny, J. *et al.* The antibody aducanumab reduces Aβ plaques in Alzheimer's disease. *Nature 2016 537:7618* **537**, 50–56 (2016).
19. Ruparelia, A. A. *et al.* The African killifish: A short-lived vertebrate model to study the biology of sarcopenia and longevity. *Aging Cell* **23**, e13862 (2024).

20. Di Cicco, E., Tozzini, E. T., Rossi, G. & Cellerino, A. The short-lived annual fish Nothobranchius furzeri shows a typical teleost aging process reinforced by high incidence of age-dependent neoplasias. *Exp Gerontol* **46**, 249–256 (2011).
21. Reichard, M. *et al.* Lifespan and telomere length variation across populations of wild-derived African killifish. *Mol Ecol* **31**, 5979–5992 (2022).
22. Hartmann, N. *et al.* Telomeres shorten while Tert expression increases during ageing of the short-lived fish Nothobranchius furzeri. *Mech Ageing Dev* **130**, 290–296 (2009).
23. Wendler, S., Hartmann, N., Hoppe, B. & Englert, C. Age-dependent decline in fin regenerative capacity in the short-lived fish Nothobranchius furzeri. *Aging Cell* **14**, (2015).
24. Van houcke, J. *et al.* Aging impairs the essential contributions of non-glial progenitors to neurorepair in the dorsal telencephalon of the Killifish Nothobranchius furzeri. *Aging Cell* **20**, (2021).
25. Morabito, G., Ryabova, A. & Valenzano, D. R. Immune aging in annual killifish. *Immun Ageing* **21**, 18 (2024).
26. Bradshaw, W. J., Poeschla, M., Placzek, A., Kean, S. & Valenzano, D. R. Extensive age-dependent loss of antibody diversity in naturally short-lived turquoise killifish. *Elife* **11**, (2022).
27. Morabito, G. *et al.* Spontaneous onset of cellular markers of inflammation and genome instability during aging in the immune niche of the naturally short-lived turquoise killifish (Nothobranchius furzeri). *bioRxiv* 2023.02.06.527346 (2023) doi:10.1101/2023.02.06.527346.
28. Kelmer Sacramento, E. *et al.* Reduced proteasome activity in the aging brain results in ribosome stoichiometry loss and aggregation. *Mol Syst Biol* (2020) doi:10.15252/msb.20209596.
29. Matsui, H., Kenmochi, N. & Namikawa, K. Age- and α-Synuclein-Dependent Degeneration of Dopamine and Noradrenaline Neurons in the Annual Killifish Nothobranchius furzeri. *Cell Rep* **26**, 1727-1733.e6 (2019).
30. Louka, A. *et al.* New lessons on TDP-43 from old N. furzeri killifish. *Aging Cell* **21**, (2022).
31. Chen, Y. R. *et al.* Tissue-specific landscape of protein aggregation and quality control in an aging vertebrate. *Dev Cell* **0**, (2024).
32. Harel, I. *et al.* Identification of protein aggregates in the aging vertebrate brain with prion-like and phase-separation properties. *Cell Rep* **43**, (2024).
33. Di Fraia, D. *et al.* Impaired biogenesis of basic proteins impacts multiple hallmarks of the aging brain. *bioRxiv* (2024) doi:10.1101/2023.07.20.549210.
34. Tozzini, E. T., Baumgart, M., Battistoni, G. & Cellerino, A. Adult neurogenesis in the short-lived teleost Nothobranchius furzeri: Localization of neurogenic niches, molecular characterization and effects of aging. *Aging Cell* **11**, 241–251 (2012).
35. Vanhunsel, S. *et al.* The killifish visual system as an in vivo model to study brain aging and rejuvenation. *NPJ Aging Mech Dis* **7**, (2021).
36. Baumgart, M. *et al.* Longitudinal RNA-Seq Analysis of Vertebrate Aging Identifies Mitochondrial Complex I as a Small-Molecule-Sensitive Modifier of Lifespan. *Cell Syst* **2**, 122–132 (2016).

890 37. Bagnoli, S., Fronte, B., Bibbiani, C., Terzibasi Tozzini, E. & Cellerino, A. Quantification
891 of noradrenergic-, dopaminergic-, and tectal-neurons during aging in the short-lived
892 killifish Nothobranchius furzeri. *Aging Cell* **21**, (2022).
893 38. Terzibasi, E. *et al.* Large differences in aging phenotype between strains of the short-lived
894 annual fish Nothobranchius furzeri. *PLoS One* **3**, (2008).
895 39. Valenzano, D. R. *et al.* Resveratrol prolongs lifespan and retards the onset of age-related
896 markers in a short-lived vertebrate. *Current Biology* **16**, 296–300 (2006).
897 40. McKay, A. *et al.* An automated feeding system for the African killifish reveals effects of
898 dietary restriction on lifespan and allows scalable assessment of associative learning. *Elife*
899 **11**, (2022).
900 41. Valenzano, D. R., Terzibasi, E., Cattaneo, A., Domenici, L. & Cellerino, A. Temperature
901 affects longevity and age-related locomotor and cognitive decay in the short-lived fish:
902 Nothobranchius furzeri. *Aging Cell* **5**, 275–278 (2006).
903 42. Bergmans, S., Raes, L., Moons, L. & De Groef, L. A review on neurodegeneration in the
904 fast-ageing killifish, the first animal model to study the natural occurrence of neuronal cell
905 loss. *Ageing Res Rev* **91**, (2023).
906 43. Scheidt, H. A. *et al.* Pyroglutamate-Modified Amyloid β (11- 40) Fibrils Are More Toxic
907 than Wildtype Fibrils but Structurally Very Similar. *Chemistry - A European Journal* **23**,
908 15834–15838 (2017).
909 44. Bayer, T. A. Pyroglutamate Aβ cascade as drug target in Alzheimer's disease. *Molecular*
910 *Psychiatry 2021 27:4* **27**, 1880–1885 (2021).
911 45. D'Angelo, L. Brain atlas of an emerging teleostean model: Nothobranchius furzeri.
912 *Anatomical Record* **296**, 681–691 (2013).
913 46. Jucker, M. *et al.* Age-related deposition of glia-associated fibrillar material in brains of
914 C57BL/6 mice. *Neuroscience* **60**, 875–889 (1994).
915 47. Jucker, M. *et al.* Age-associated inclusions in normal and transgenic mouse brain. *Science*
916 **255**, 1443–1445 (1992).
917 48. Crowhurst, M. O., Layton, J. & Lieschke, G. Developmental biology of zebrafish myeloid
918 cells. *International Journal of Developmental Biology* (2002)
919 doi:10.1387/IJDB.12141435.
920 49. LaFerla, F. M., Green, K. N. & Oddo, S. Intracellular amyloid-β in Alzheimer's disease.
921 *Nature Reviews Neuroscience 2007 8:7* **8**, 499–509 (2007).
922 50. Wegiel, J. *et al.* Intraneuronal Abeta immunoreactivity is not a predictor of brain
923 amyloidosis-beta or neurofibrillary degeneration. *Acta Neuropathol* **113**, 389–402 (2007).
924 51. Oddo, S., Caccamo, A., Smith, I. F., Green, K. N. & LaFerla, F. M. A Dynamic
925 Relationship between Intracellular and Extracellular Pools of Aβ. *Am J Pathol* **168**, 184
926 (2006).
927 52. Mori, C. *et al.* Intraneuronal Aβ42 accumulation in Down syndrome brain. *Amyloid* **9**, 88–
928 102 (2002).
929 53. Gyure, K. A., Durham, R., Stewart, W. F., Smialek, J. E. & Troncoso, J. C. Intraneuronal
930 abeta-amyloid precedes development of amyloid plaques in Down syndrome. *Arch Pathol*
931 *Lab Med* **125**, 489–492 (2001).
932 54. Lee, J. H. *et al.* Faulty autolysosome acidification in Alzheimer's disease mouse models
933 induces autophagic build-up of Aβ in neurons, yielding senile plaques. *Nature*
934 *Neuroscience 2022 25:6* **25**, 688–701 (2022).

935 55. Sullivan, C. P. *et al.* Pyroglutamate-Aβ 3 and 11 colocalize in amyloid plaques in
936 Alzheimer's disease cerebral cortex with pyroglutamate-Aβ 11 forming the central core.
937 *Neurosci Lett* **505**, 109–112 (2011).
938 56. Xue, C., Lin, T. Y., Chang, D. & Guo, Z. Thioflavin T as an amyloid dye: fibril
939 quantification, optimal concentration and effect on aggregation. *R Soc Open Sci* **4**, (2016).
940 57. Scior, A. *et al.* Complete suppression of Htt fibrilization and disaggregation of Htt fibrils
941 by a trimeric chaperone complex. *EMBO J* **37**, 282–299 (2018).
942 58. Banote, R. K. *et al.* Amyloid precursor protein-b facilitates cell adhesion during early
943 development in zebrafish. *Sci Rep* **10**, (2020).
944 59. Samali, A., Cai, J., Zhivotovsky, B., Jones, D. P. & Orrenius, S. *Presence of a Pre-*
945 *Apoptotic Complex of pro-Caspase-3, Hsp60 and Hsp10 in the Mitochondrial Fraction of*
946 *Jurkat Cells*. *The EMBO Journal* vol. 18 (1999).
947 60. Piront, M. L. & Schmidt, R. Inhibition of long-term memory formation by anti-ependymin
948 antisera after active shock-avoidance learning in goldfish. *Brain Res* **442**, 53–62 (1988).
949 61. Inhibition of memory consolidation by antibodies against cell adhesion molecules after
950 active avoidance conditioning in zebrafish - PubMed.
951 https://pubmed.ncbi.nlm.nih.gov/10235674/.
952 62. Lin, X. *et al.* c-Fos mapping of brain regions activated by multi-modal and electric foot
953 shock stress. *Neurobiol Stress* **8**, 92–102 (2018).
954 63. Lara Aparicio, S. Y. *et al.* Current Opinion on the Use of c-Fos in Neuroscience. *NeuroSci*
955 **3**, 687–702 (2022).
956 64. Calvo, R., Hofmann, M. H. & Schluessel, V. Brain areas activated during visual learning
957 in the cichlid fish Pseudotropheus zebra. *Brain Struct Funct* **228**, 859–873 (2023).
958 65. Rodrigue, K. M., Kennedy, K. M. & Park, D. C. Beta-amyloid deposition and the aging
959 brain. *Neuropsychology Review* vol. 19 436–450 Preprint at
960 https://doi.org/10.1007/s11065-009-9118-x (2009).
961 66. Maloney, J. A. *et al.* Molecular Mechanisms of Alzheimer Disease Protection by the
962 A673T Allele of Amyloid Precursor Protein. *J Biol Chem* **289**, 30990 (2014).
963 67. Jonsson, T. *et al.* A mutation in APP protects against Alzheimer's disease and age-related
964 cognitive decline. *Nature 2012 488:7409* **488**, 96–99 (2012).
965 68. Cui, R. *et al.* Relaxed Selection Limits Lifespan by Increasing Mutation Load. *Cell* **178**,
966 385-399.e20 (2019).
967 69. Hartlage-Rübsamen, M. *et al.* Glutaminyl cyclase contributes to the formation of focal and
968 diffuse pyroglutamate (pGlu)-Aβ deposits in hippocampus via distinct cellular
969 mechanisms. *Acta Neuropathol* **121**, 705–719 (2011).
970 70. Wittnam, J. L. *et al.* Pyroglutamate Amyloid β (Aβ) Aggravates Behavioral Deficits in
971 Transgenic Amyloid Mouse Model for Alzheimer Disease. *J Biol Chem* **287**, 8154 (2012).
972 71. Burrinha, T. *et al.* Upregulation of APP endocytosis by neuronal aging drives amyloid-
973 dependent synapse loss. *J Cell Sci* **134**, (2021).
974 72. Huse, J. T. *et al.* β-secretase processing in the trans-Golgi network preferentially generates
975 truncated amyloid species that accumulate in Alzheimer's disease brain. *Journal of*
976 *Biological Chemistry* **277**, 16278–16284 (2002).
977 73. Lu, L. & Hong, W. From endosomes to the trans-Golgi network. *Semin Cell Dev Biol* **31**,
978 30–39 (2014).
979 74. Saimani, U. & Kim, K. Traffic from the endosome towards trans-Golgi network. *Eur J*
980 *Cell Biol* **96**, 198–205 (2017).

75. He, W. & Barrow, C. J. The A beta 3-pyroglutamyl and 11-pyroglutamyl peptides found in senile plaque have greater beta-sheet forming and aggregation propensities in vitro than full-length A beta. *Biochemistry* **38**, 10871–10877 (1999).
76. Luheshi, L. M. *et al.* Sequestration of the Aβ peptide prevents toxicity and promotes degradation in vivo. *PLoS Biol* **8**, (2010).
77. Wang, S. *et al.* Amyloid β precursor protein regulates neuron survival and maturation in the adult mouse brain. *Molecular and Cellular Neuroscience* **77**, 21–33 (2016).
78. Zheng, H. *et al.* beta-Amyloid precursor protein-deficient mice show reactive gliosis and decreased locomotor activity. *Cell* **81**, 525–531 (1995).
79. Senechal, Y., Kelly, P. H. & Dev, K. K. Amyloid precursor protein knockout mice show age-dependent deficits in passive avoidance learning. *Behavioural Brain Research* **186**, 126–132 (2008).
80. Morley, J. E., Farr, S. A., Nguyen, A. D. & Xu, F. What is the Physiological Function of Amyloid-Beta Protein? *Journal of Nutrition, Health and Aging* **23**, 225–226 (2019).
81. Glasauer, S. M. K. & Neuhauss, S. C. F. Whole-genome duplication in teleost fishes and its evolutionary consequences. *Molecular Genetics and Genomics* **289**, 1045–1060 (2014).
82. Naumann, U., Brazzell, J. L., Crim, M. J. & Hoppe, B. Comprehensive Colony Health Management and Emerging Pathogens of the Annual Killifish Species Nothobranchius furzeri. *J Am Assoc Lab Anim Sci* **63**, 20–33 (2024).
83. Abramson, J. *et al.* Accurate structure prediction of biomolecular interactions with AlphaFold 3. *Nature 2024 630:8016* **630**, 493–500 (2024).
84. Pettersen, E. F. *et al.* UCSF ChimeraX: Structure visualization for researchers, educators, and developers. *Protein Sci* **30**, 70–82 (2021).
85. Bentley, D. R. *et al.* Accurate whole human genome sequencing using reversible terminator chemistry. *Nature* **456**, 53–59 (2008).
86. Willemsen, D., Cui, R., Reichard, M. & Valenzano, D. R. Intra-species differences in population size shape life history and genome evolution. *Elife* **9**, 1–26 (2020).
87. Robinson, M. D., McCarthy, D. J. & Smyth, G. K. edgeR: a Bioconductor package for differential expression analysis of digital gene expression data. *Bioinformatics* **26**, 139–140 (2010).
88. Huang, D. W., Sherman, B. T. & Lempicki, R. A. Systematic and integrative analysis of large gene lists using DAVID bioinformatics resources. *Nature Protocols 2009 4:1* **4**, 44–57 (2008).
89. Elagoz, A. M. *et al.* Optimization of Whole Mount RNA Multiplexed in situ Hybridization Chain Reaction With Immunohistochemistry, Clearing and Imaging to Visualize Octopus Embryonic Neurogenesis. *Front Physiol* **13**, 882413 (2022).
90. Choi, H. M. T. *et al.* Third-generation in situ hybridization chain reaction: multiplexed, quantitative, sensitive, versatile, robust. *Development* **145**, (2018).

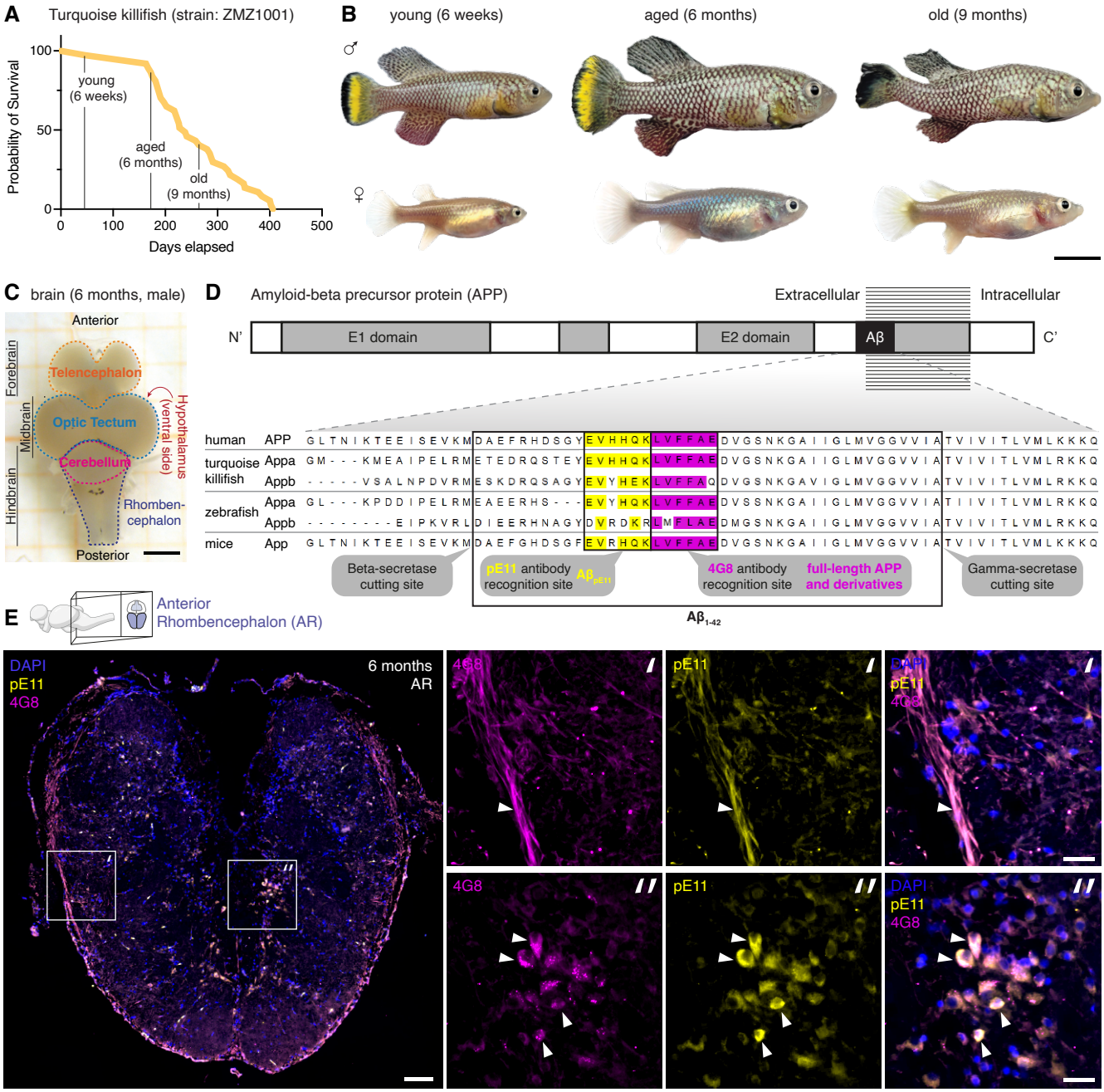

Figure 1. Amyloid beta is evolutionary conserved between turquoise killifish and humans and is expressed in the turquoise killifish brain. (**A**) Survival curve for the turquoise killifish strain ZMZ1001. (**B**) Representative pictures of male and female fish at different ages. Scalebar represents 1 cm. (**C**) Representative brain (6-month-old male) with annotated brain regions. Scalebar represents 1 mm. (**D**) Graphical representation of the amyloid beta precursor protein (APP) and amino acid sequences of APP precursors across four species. Amino acid residues are colored according to their physicochemical properties (ZAPPO): aliphatic/hydrophobic (residues ILVAM) - rose, aromatic (FWY) - orange, positive (KRH) - dark blue, negative (DE) - red, hydrophilic (STNQ) - light green, conformationally special (PG) - magenta, cysteine (C) - yellow. (**E**) Immunohistochemistry staining in the 6-month-old anterior rhombencephalon (AR) using the pE11 and 4G8 antibodies, targeting $A\beta_{pE11\text{-}42}$ (yellow) and APP-derivatives (magenta), respectively. Arrowheads indicate $pE11^{+}/4G8^{+}$ signal. Scalebars represent 100 μm in the overview and 25 μm in the zoom-ins.

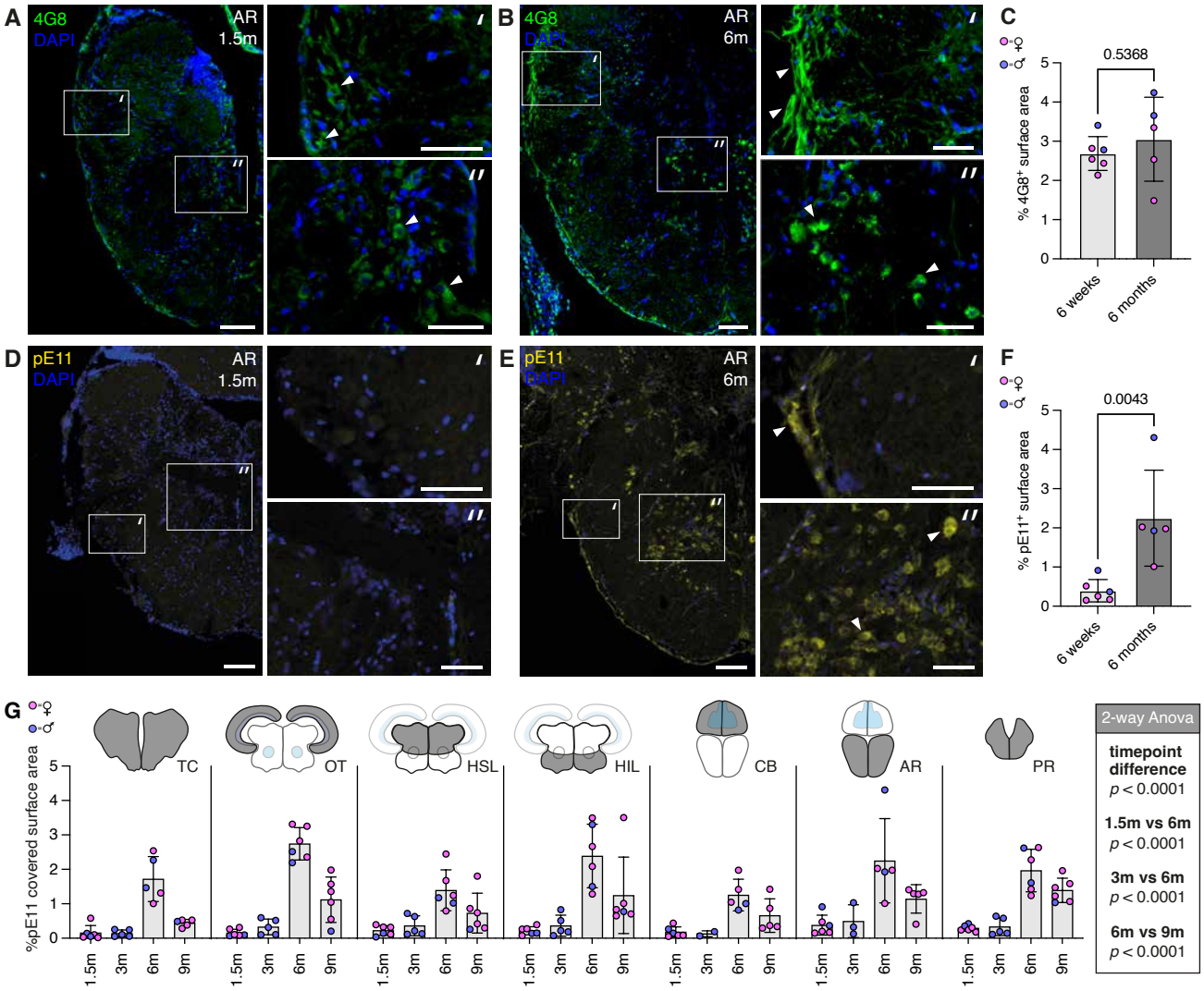

Figure 2. pE11 signal accumulates in an age-dependent manner across the rostro-caudal axis of the turquoise killifish brain. (**A, B**) Immunohistochemistry staining using the 4G8 antibody in the anterior rhombencephalon (AR) of young (6-week-old) and aged (6-month-old) killifish. (**C**) Quantification of the percentage of 4G8-covered surface area in 6-week-old and 6-month-old AR regions. (**D, E**) Immunohistochemistry staining using the pE11 antibody in the anterior rhomboencephalon (AR) of young (6-week-old) and aged (6-month-old) killifish. (**F**) Quantification of the percentage of pE11-covered surface area in 6-week-old and 6-month-old AR regions. (A, B, D, E) Scale bars represent 100 µm in the overview and 50 µm in the zoom-in. Arrowheads indicate positive signal. (C, F) Significance was calculated using a Mann-Whitney test. Error bars represent standard deviation. (**G**) Quantification of the percentage of pE11-covered surface area across seven different brain regions at four different time points, including the telencephalon (TC), optic tectum (OT), hypothalamus superior lobe (HSL), hypothalamus inferior lobe (HIL), cerebellum (CB), anterior rhombencephalon (AR) and posterior rhombencephalon (PR). Error bars represent standard deviation. Significances were calculated using a 2-way Anova test, including a multiple comparison test to investigate the difference between 1.5-months and 6-months, 3-months and 6-months as well as 6-months and 9-months.

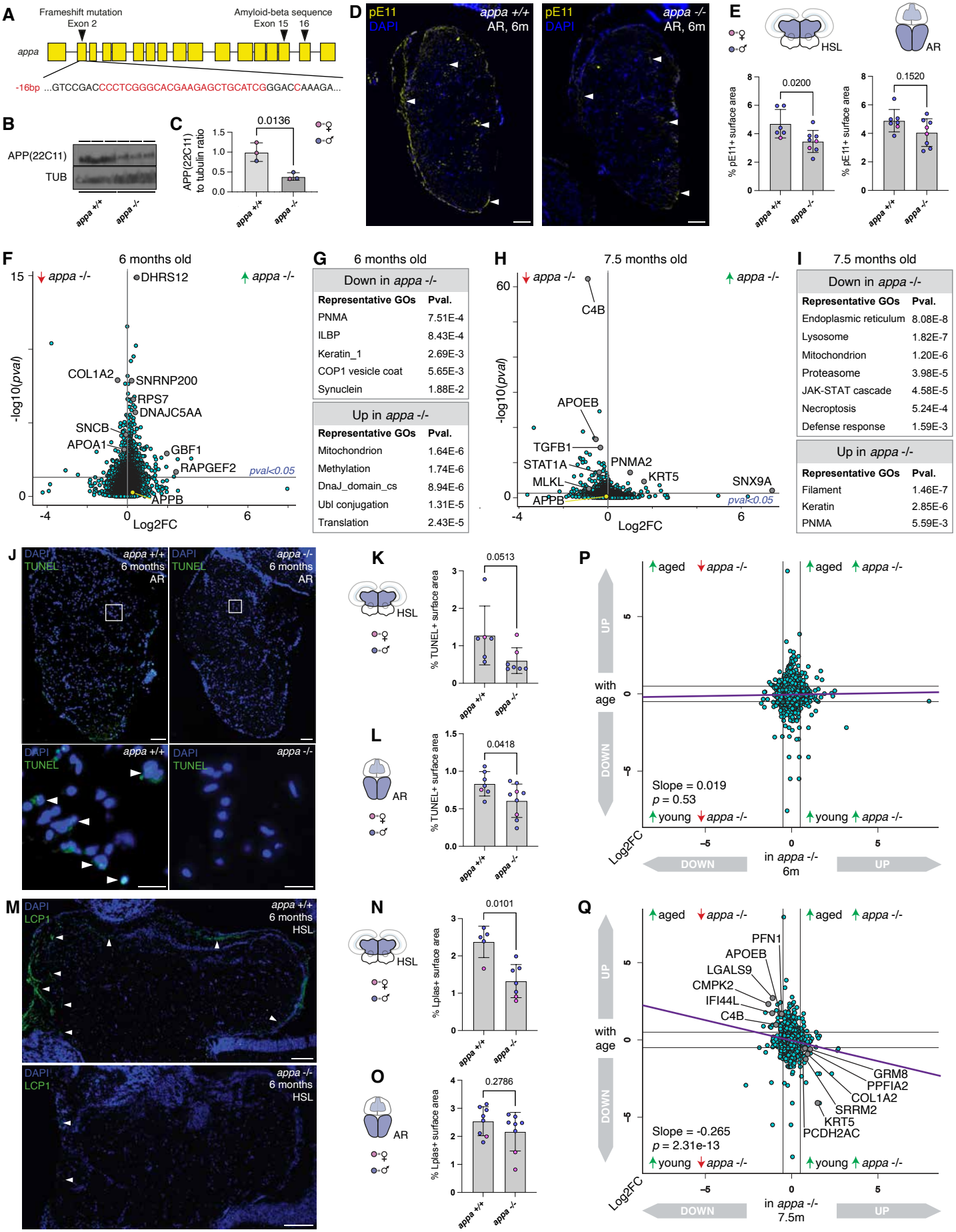

Figure 3. *appa* knock-out mitigates killifish brain aging including cell death and inflammation. (**A**) Schematic representation of the killifish *appa* gene, indicating the mutation site on exon 2, as well as highlighting the location of the amyloid beta coding region in exons 15 and 16.

(**B**) Western blot on turquoise killifish lysates from 6-month-old killifish using APP(22C11) and alpha-tubulin targeting antibodies. (**C**) Quantification of western blot results, depicting the APP(22C11) to tubulin ratio. Significance was calculated using a Mann-Whitney test. (**D**) Representative immunohistochemistry staining results using the pE11 antibody (yellow) in the anterior rhombencephalon (AR) of wild-type and *appa* -/- brains. Arrowheads indicate pE11$^+$ signal. Scale bar represents 100 μm. (**E**) Quantification of the percentage of pE11 covered surface area in hypothalamus superior lobe (HSL) and anterior rhomboencephalon (AR) regions of 6-month-old individuals. Significance was calculated using a Mann-Whitney test. Error bars represent standard deviation. (**F**) Volcano plot displaying differences in brain protein abundance between *appa* -/- and their wild-type siblings (6-month-old, 3 males and 3 females per genotype). Differentially abundant proteins are highlighted, representing relevant biological processes. Vertical red line indicates log2FC of 0. (**G**) Representative gene ontologies produced from the differentially abundant proteins between 6-month-old *appa* -/- mutants and their wild-type siblings (pval < 0.05). (**H**) Volcano plot displaying differences in brain protein abundance between *appa* -/- mutants and their wild-type siblings (7.5-month-old, 3 males and 3 females per genotype). Differentially abundant proteins are highlighted, representing relevant biological processes. Vertical red line indicates log2FC of 0. (**I**) Representative gene ontologies produced from the differentially abundant proteins between 7.5-month-old *appa* -/- mutants and their wild-type siblings (pval < 0.05). (**J**) Representative TUNEL (green) staining results in the anterior rhombencephalon (AR) of wild-type and *appa* -/- mutant brains. Arrowheads indicate TUNEL$^+$ signal. Scale bar represents 100 μm in the overview and 20 μm in the zoom-ins. (**K, L**) Quantification of the percentage of TUNEL$^+$-covered surface area in hypothalamus superior lobe (K) and anterior rhomboencephalon (L) regions of 6-month-old individuals. Significance was calculated using a Mann-Whitney test. Error bars represent standard deviation. (**M**) Representative immunohistochemistry staining results using the LCP1 antibody (green) in the hypothalamus superior lobe (HSL) of wild-type and *appa* -/- brains. Arrowheads indicate LCP1$^+$ signal. Scale bar represents 100 μm. (**N, O**) Quantification of the percentage of LCP1$^+$-covered surface area in hypothalamus superior lobe (N) and anterior rhombencephalon (O) regions of 6-month-old individuals (3 male, 3 female). Significance was calculated using a Mann-Whitney test. Error bars represent standard deviation. (**P, Q**) Proteome-wide comparison between the log2FC of proteins up or downregulated in 6-months-old brains compared to 6-weeks-old brains (y-axis), plotted against the log2FC describing the up and downregulation of proteins in the appa mutant compared to the same aged wild-type siblings at 6-months (P) and 7.5 months (Q).

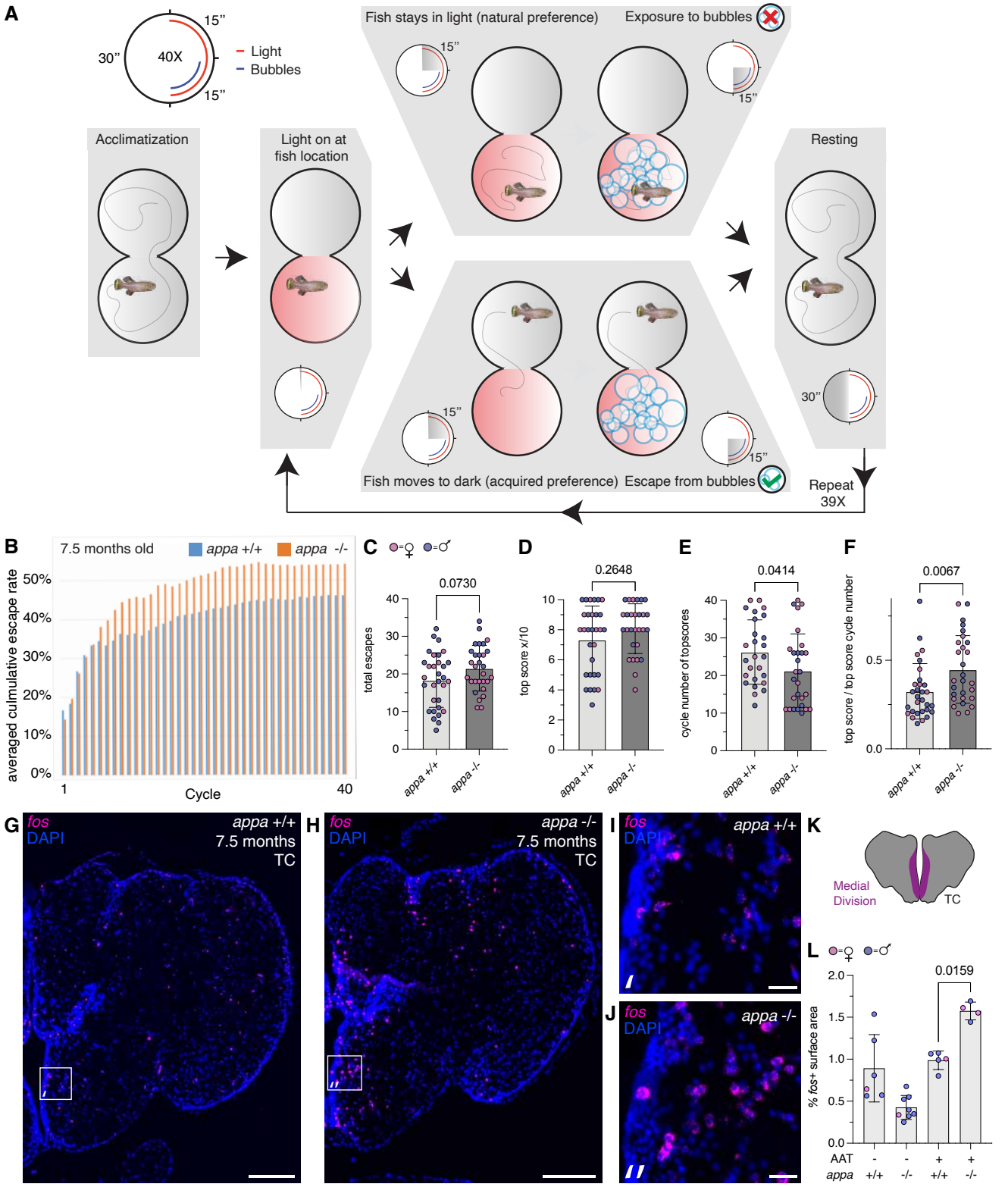

Figure 4. *appa* knock-out mitigates age-related learning deficit in turquoise killifish. (**A**) Experimental set-up of the performed active avoidance test (AAT). (**B**) Plot describing the averaged cumulative escape rate of 7.5-month-old *appa* -/- mutants (orange, n = 28 fish) and their wild-type siblings (blue, n = 30 fish) across 40 cycles. (**C-F**) Quantification of four behavioral traits, compared between 7.5-month-old *appa* -/- mutants and their wild-type siblings. These traits include (**C**) the total escape rate (n/40 cycles), (**D**) the top score of the fish within a window of ten consecutive cycles representing the extent of learning, (**E**) the cycle number at which top scores were reached (excluding non-learners (n=4) defined by total escapes < 10) representing the speed of learning, and (**F**) a combined value in which both the extent and speed of learning were considered (top scores / cycle number at which top scores were reached). Significance values were calculated through Mann-Whitney testing. (**G-J**) Hybridizing Chain Reaction (HCR) staining against *fos* transcripts (magenta), marking neurons involved in active learning within the telencephalon (TC) of *appa* mutants (**H,J**) and their wild-type siblings (**G,I**). Scale bars represent 200 μm in the overview and 20 μm in the zoom-ins. (**K**) Schematic representation of the medial division (magenta) within the telencephalon (TC). (**L**) Quantification of the percentage of *fos*+ surface area in the medial division of the telencephalon of 6-month-old *appa* -/- mutant fish and their wild-type siblings that have not been subjected to an active avoidance test (AAT -), as well as as 7.5-month-old *appa* -/- mutant fish and their wild-type siblings which were subjected to an active avoidance test (AAT +). Significance value was calculated through a Mann-Whitney test.

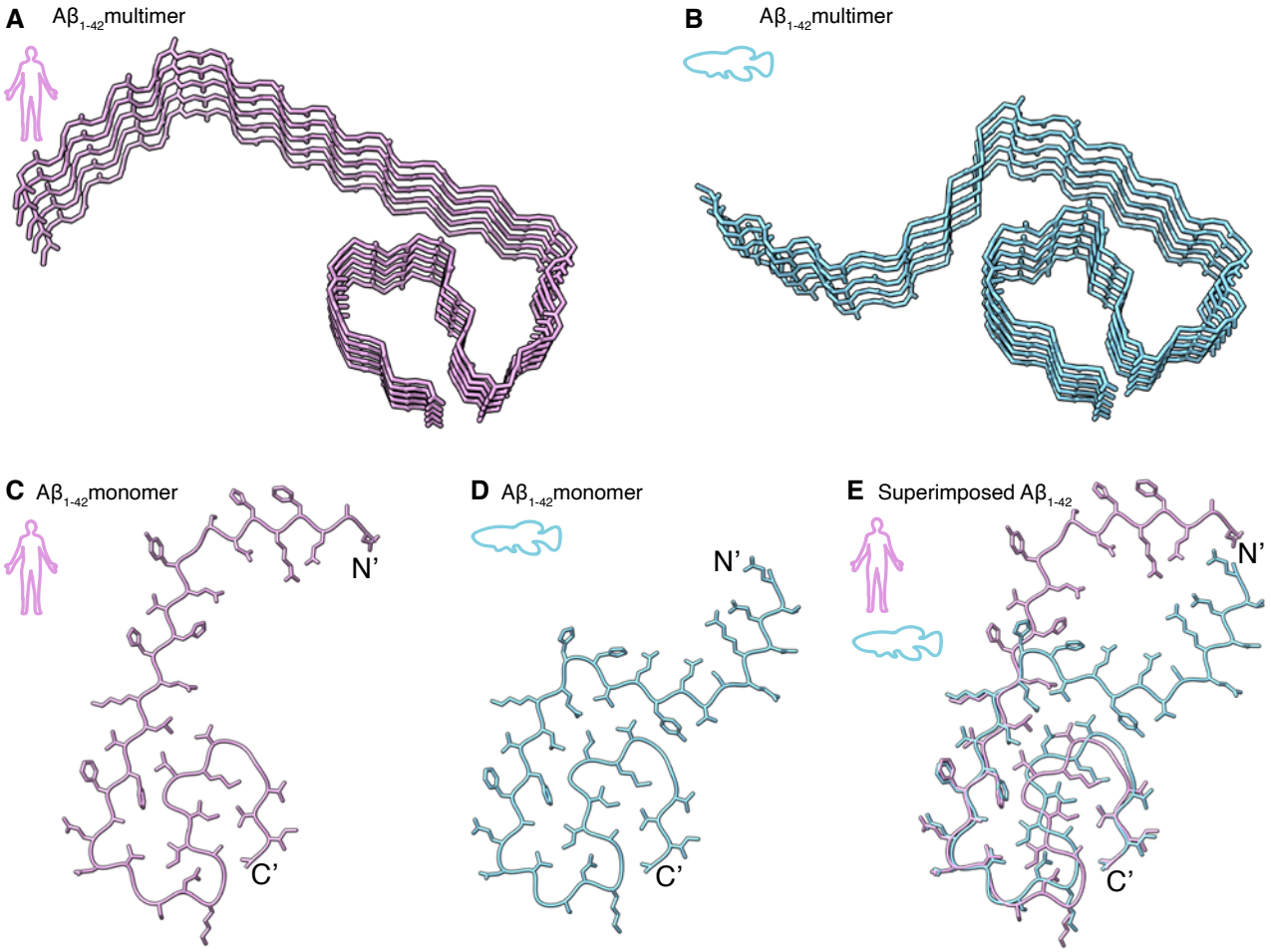

Figure S1. 3D protein structure of amyloid beta (1-42) is conserved between turquoise killifish and humans. (**A**) Alphafold (V3) predicted stucture of human amyloid beta (1-42) in an aggregated state. (**B**) Alphafold-predicted stucture of killifish amyloid beta (1-42) derived from *appa* in an aggregated state. (**C**) Alphafold prediction of human amyloid beta monomer 1-42), as part of the multimer shown in (A). (**D**) Alphafold prediction of turquoise killifish amyloid beta monomer (1-42) derived from *appa*, as part of the multimer shown in (B). (**E**) Superimposed of the Alphafold-predicted multimer structures (only one monomer displayed) of human (pink) and killifish (blue) amyloid beta (1-42) (backbone r.m.s.d. for residues Q15-A42: 0.859 Angstrom).

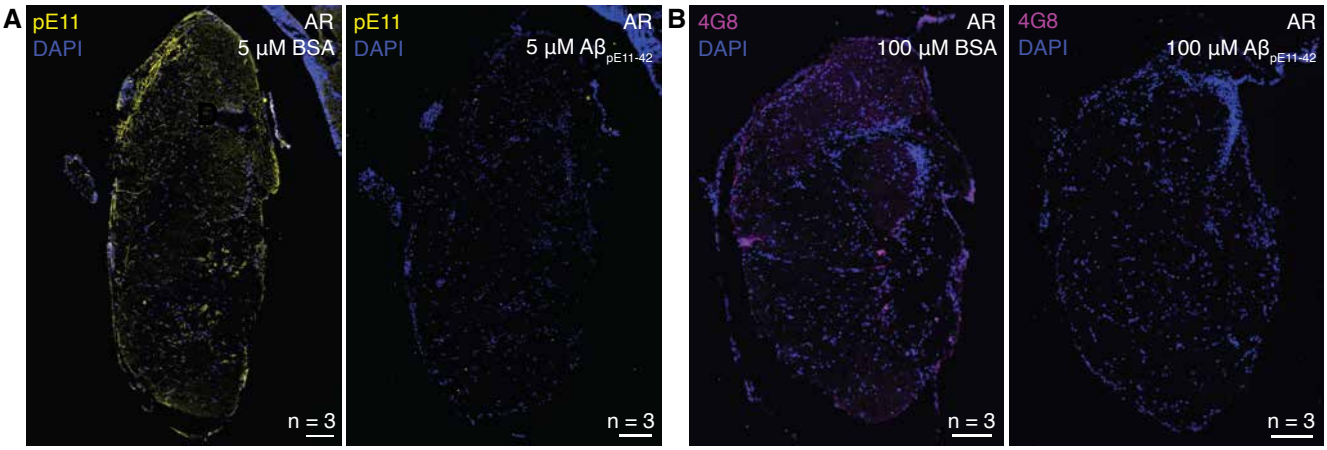

Figure S2. pE11 and 4G8 antibodies bind their targets in an epitope dependent manner. (A-B) Immunohistochemistry staining using the pE11 (A) or 4G8 (B) antibody, after a 30 minute incubation step of the primary antibody together with either BSA (left) or $A\beta_{pE11-42}$ peptide (right). The anterior rhombencephalon (AR) was stained from three 6-month-old turquoise killifish per condition. Scalebars represent 100 μm.

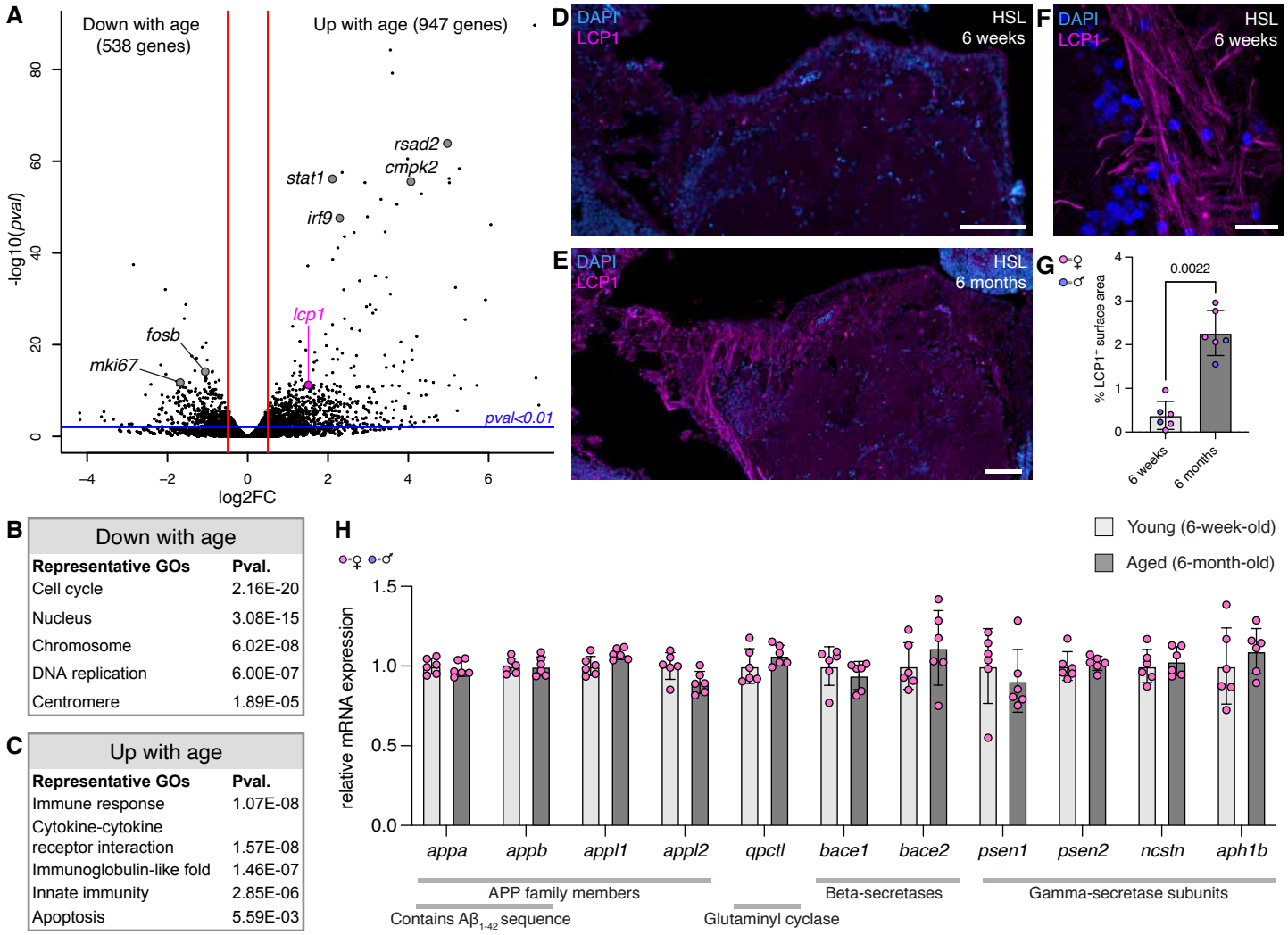

B

Down with age	
Representative GOs	**Pval.**
Cell cycle	2.16E-20
Nucleus	3.08E-15
Chromosome	6.02E-08
DNA replication	6.00E-07
Centromere	1.89E-05

C

Up with age	
Representative GOs	**Pval.**
Immune response	1.07E-08
Cytokine-cytokine receptor interaction	1.57E-08
Immunoglobulin-like fold	1.46E-07
Innate immunity	2.85E-06
Apoptosis	5.59E-03

Figure S3. The turquoise killifish brain develops an age-related inflammatory state while expressing key players of Aβ biogenesis. (**A**) Volcano plot displaying differences in gene expression levels between young (6-week-old) and aged (6-month-old) female killifish brains. Differentially expressed genes are highlighted, representing relevant biological processes. Vertical red lines indicate log2FC of (-)0.5. (**B, C**) Representative gene ontologies produced from the differentially expressed genes between young and old brains (Log2FC > 0.5 / < -0.5 and pval < 0.01). (**D, E**) Immunohistochemistry staining targeting leukocyte marker Lymphocyte Cytosolic Protein 1 (LCP1) in sections of the hypothalamus superior lobe (HSL) from a young (D) and aged (E) individual. Scale bars represent 100 μm. (**F**) High-resolution image of the HSL of a 6-month-old killifish brain, showing the striated pattern of the LCP1 staining, which reflects binding to the actin cytoskeleton. Scale bar represents 20 μm. (**G**) Quantification of the percentage of LCP1+ covered surface area in the hypothalamus of young and aged brains. Significance was calculated using a Mann-Whitney test. Error bars represent standard deviation. (**H**) Expression levels of key players in Aβ biogenesis normalized to total mRNA counts per brain, plotted as relative values to the mean value of young (6-week-old) individuals. APP = Amyloid beta Precursor Protein. Error bars represent standard deviation.

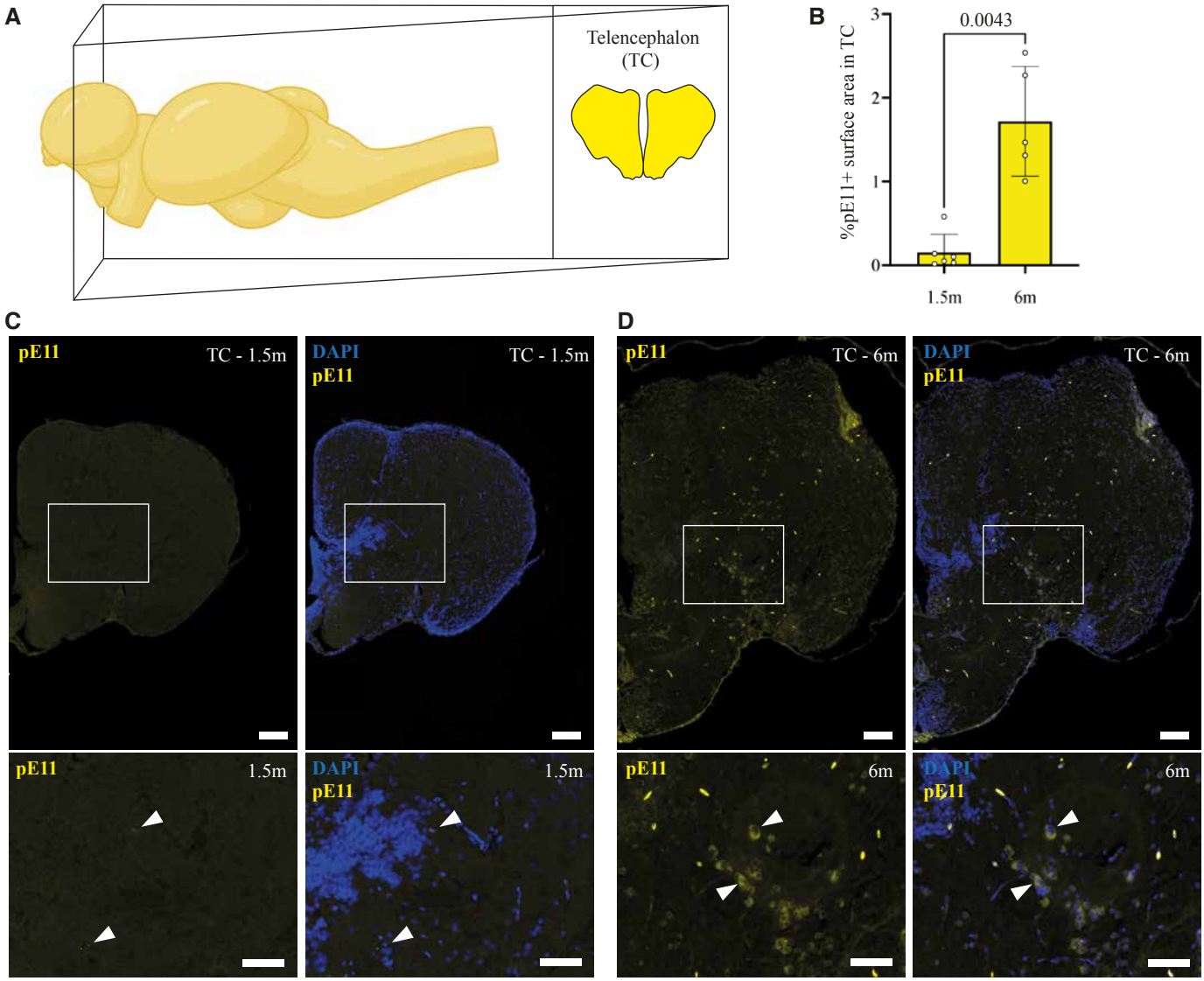

Figure S4. pE11 signal accumulates in the telencephalon in an age-dependent manner. (**A**) Schematic representation of the brain region quantified and shown in B-D. (**B**) Quantification of immunohistochemistry staining using the pE11 antibody on the telencephalon (TC) of young (6-week-old) and aged (6-month-old) killifish. Significance was calculated using a Mann-Whitney test. (**C, D**) Immunohistochemistry staining with the pE11 antibody (yellow) and DAPI (blue) in a 6-week-old (C) and 6-month-old (D) telencephalon. Arrowheads indicate examples of regions with perinuclear immunoreactivity. Scale bar represents 100 μm in the overview and 50 μm in the zoom-in.

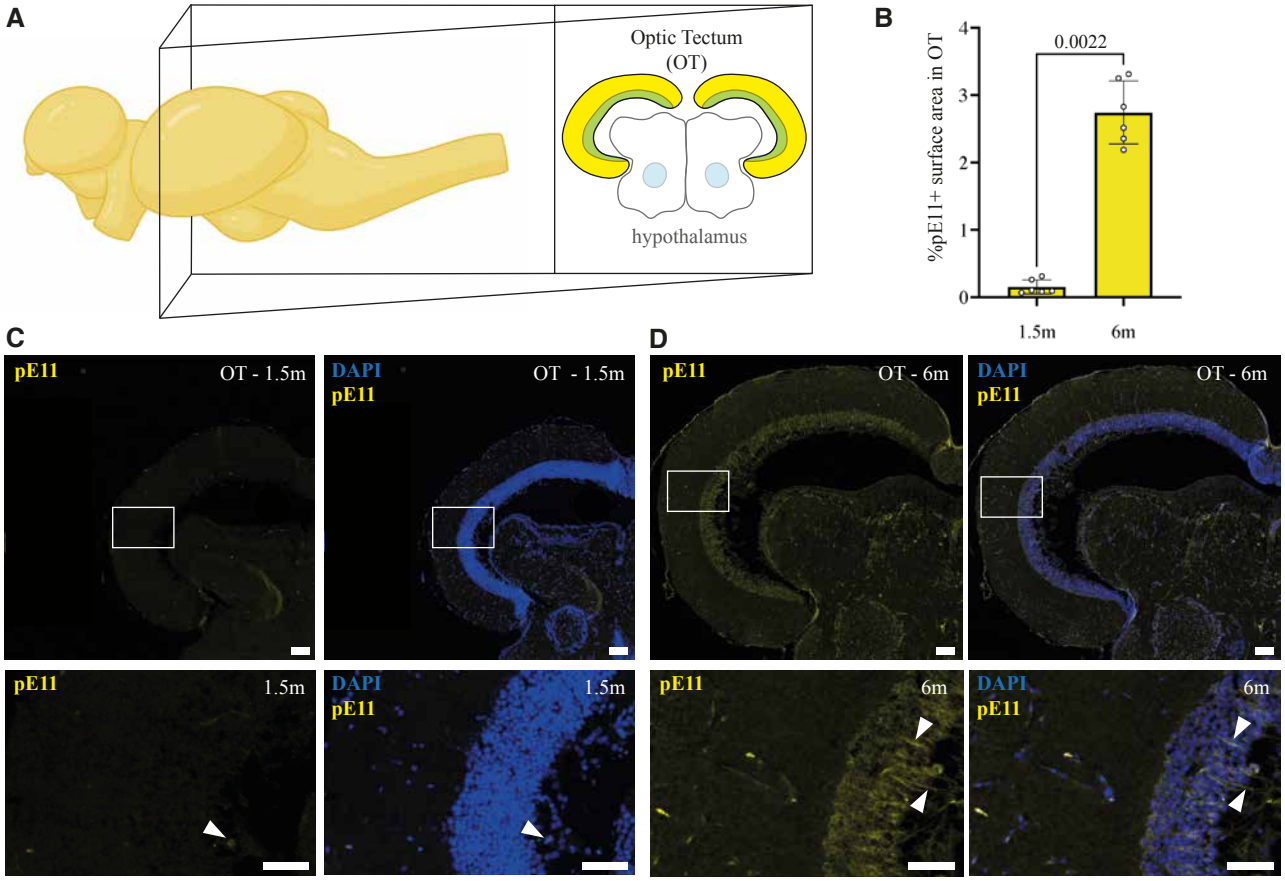

Figure S5. pE11 signal accumulates in the optic tectum in an age-dependent manner. (**A**) Schematic representation of the brain region quantified and shown in B-D. (**B**) Quantification of immunohistochemistry staining using the pE11 antibody on the optic tectum (TC) of young (6-week-old) and aged (6-month-old) killifish. Significance was calculated using a Mann-Whitney test. (**C, D**) Immunohistochemistry staining with the pE11 antibody (yellow) and DAPI (blue) in a 6-week-old (C) and 6-month-old (D) optic tectum. Arrowheads indicate regions with immunoreactivity. Scale bars represent 100 μm in the overviews and 50 μm in the zoom-ins.

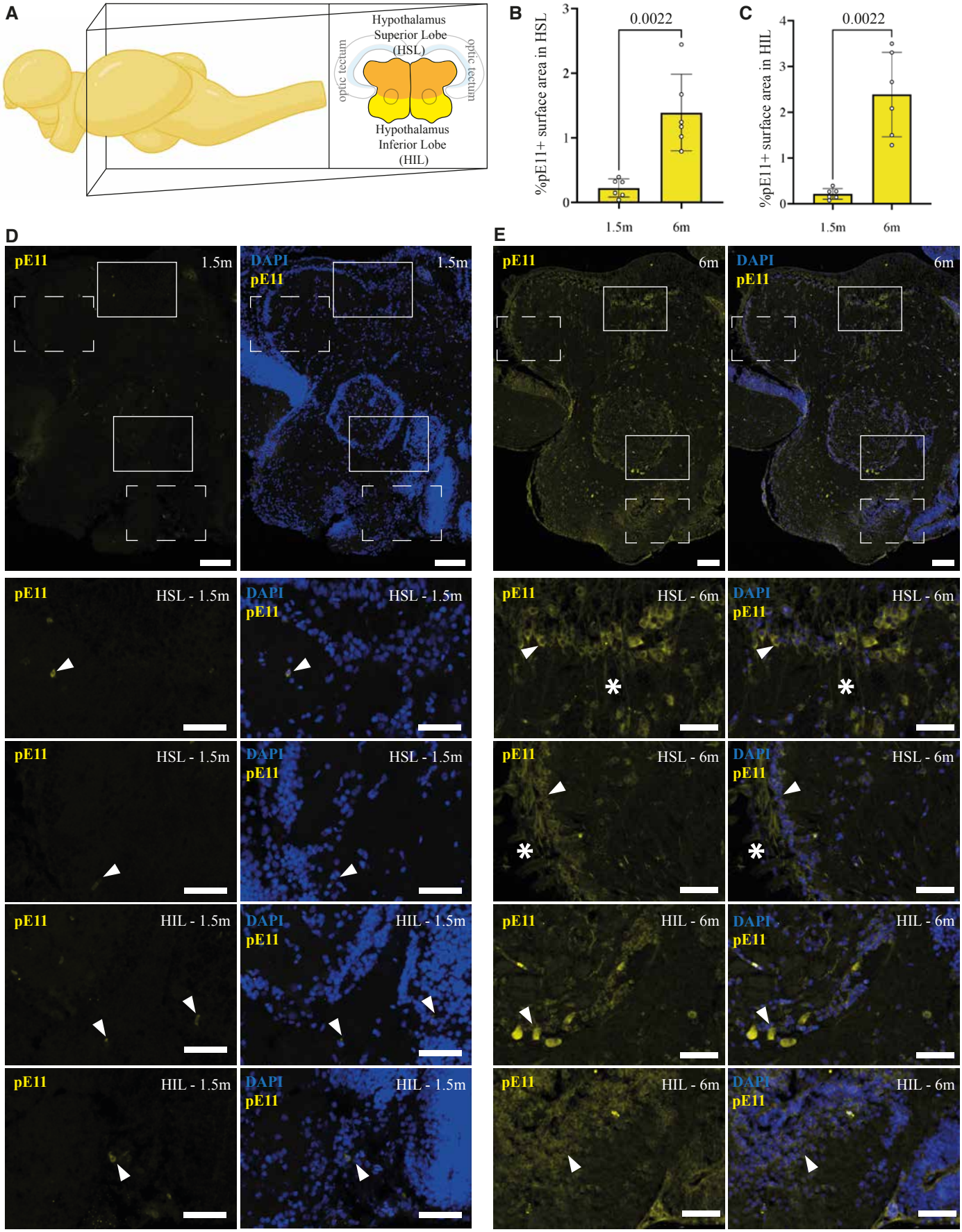

Figure S6. pE11 signal accumulates in the hypothalamus in an age-dependent manner. (**A**) Schematic representation of the brain regions quantified and shown in B-E. (**B,C**) Quantification of immunohistochemistry staining using the pE11 antibody on the hypothalamus superior lobe (HSL) and hypothalamus inferior lobe (HIL) of young (6-week-old) and aged (6-month-old) killifish. Significances were calculated using Mann-Whitney tests. (**D, E**) Immunohistochemistry staining with the pE11 antibody (yellow) and DAPI (blue) in 6-week-old (C) and 6-month-old (D) hypothalamus. Arrowheads indicate regions with perinuclear immunoreactivity. Asterisks indicate regions with filamentous immunoreactivity. Scale bars represent 100 μm in the overviews and 50 μm in the zoom-ins.

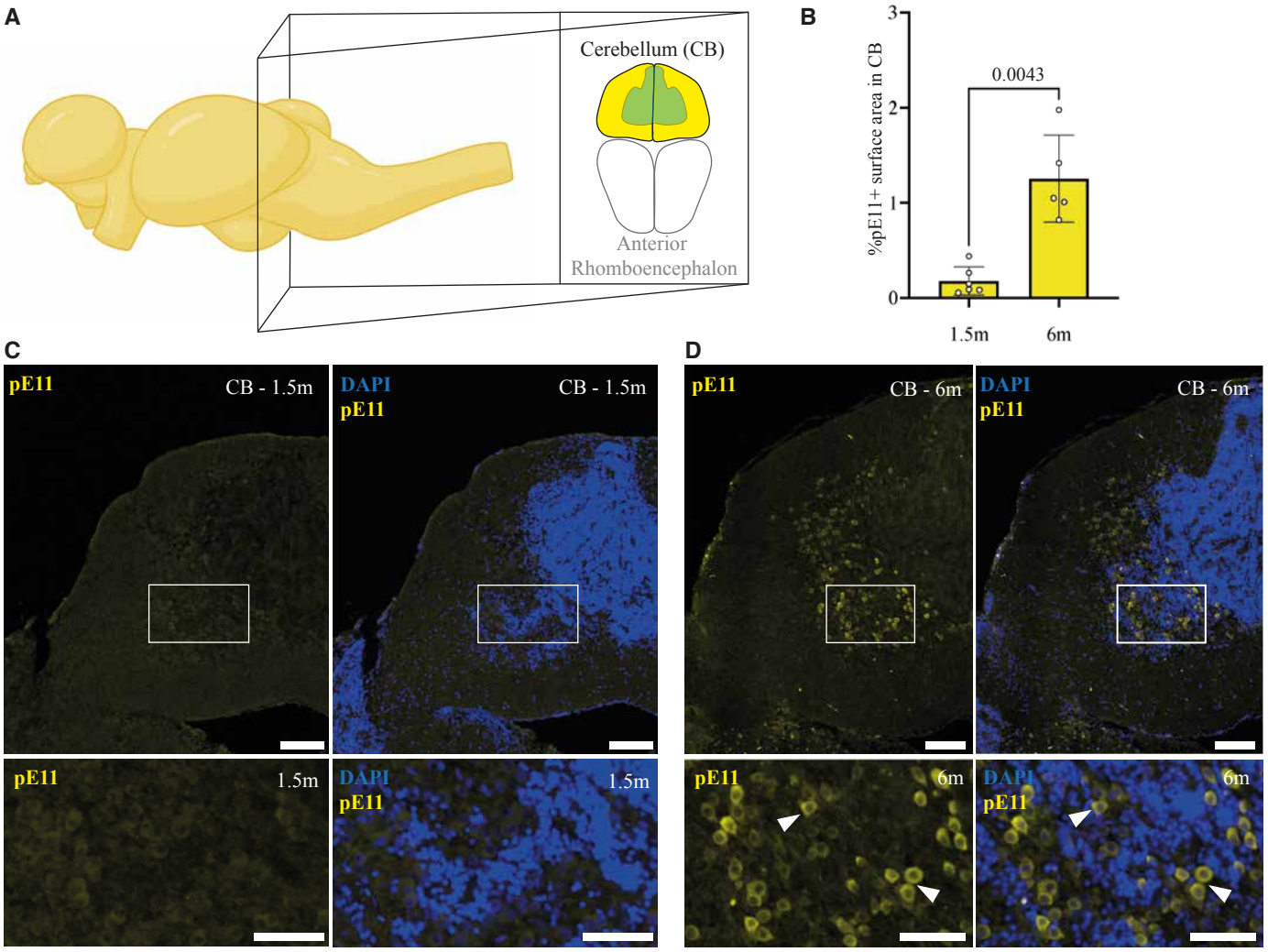

Figure S7. pE11 signal accumulates in the cerebellum in an age-dependent manner. (**A**) Schematic representation of the brain region quantified and shown in B-D. (**B**) Quantification of immunohistochemistry staining using the pE11 antibody on the cerebellum (CB) of young (6-week-old) and aged (6-month-old) killifish. Significance was calculated using a Mann-Whitney test. (**C, D**) Immunohistochemistry staining with the pE11 antibody (yellow) and DAPI (blue) in a 6-week-old (C) and 6-month-old (D) cerebellum. Arrowheads indicate examples of regions with perinuclear immunoreactivity. Scale bars represent 100 μm in the overviews and 50 μm in the zoom-ins.

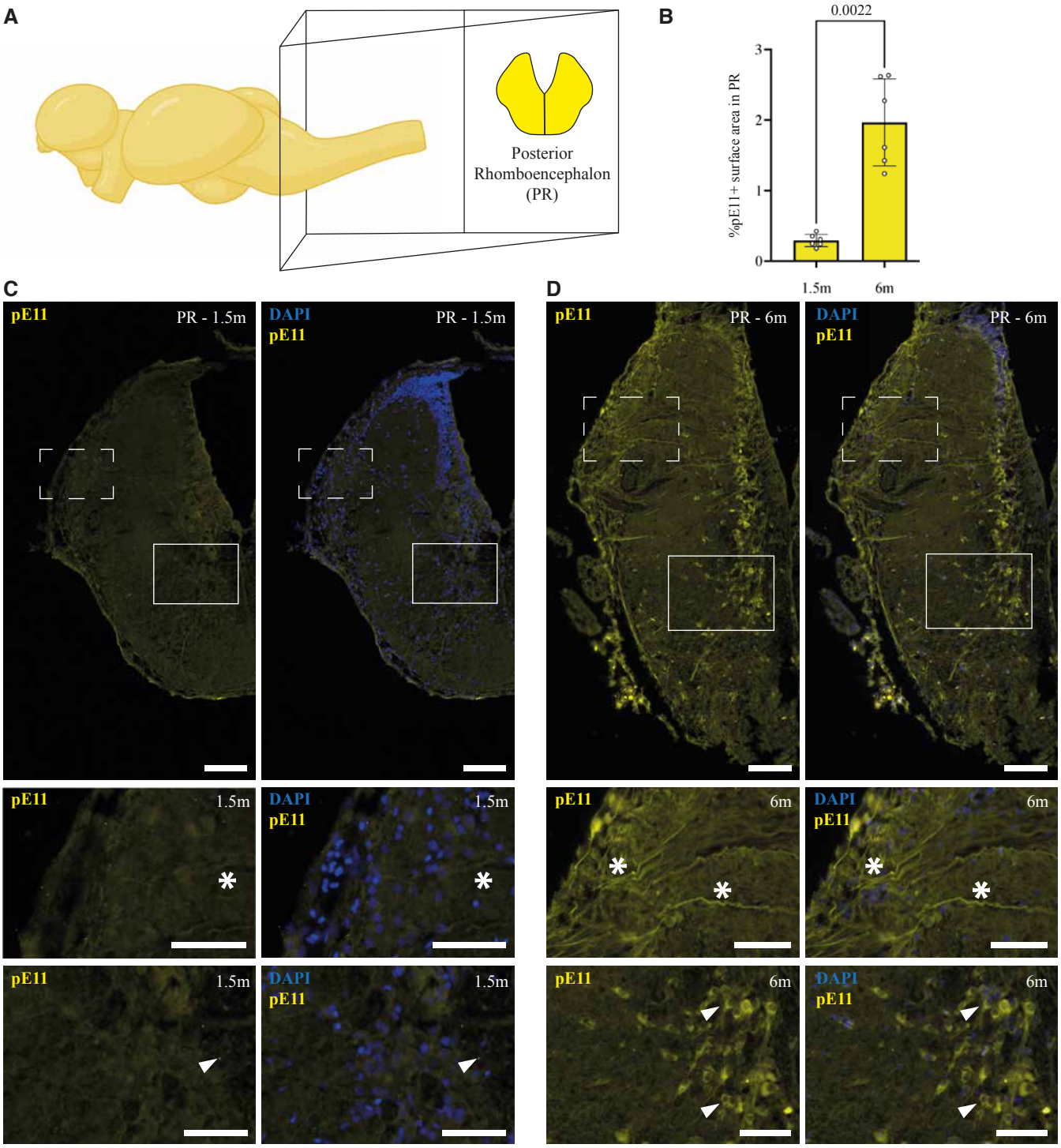

Figure S8. pE11 signal accumulates in the posterior rhomboencephalon in an age-dependent manner. (**A**) Schematic representation of the brain region quantified and shown in B-D. (**B**) Quantification of immunohistochemistry staining using the pE11 antibody on the posterior rhomboencephalon (CB) of young (6-week-old) and aged (6-month-old) killifish. Significance was calculated using a Mann-Whitney test. (**C, D**) Immunohistochemistry staining with the pE11 antibody (yellow) and DAPI (blue) in a 6-week-old (C) and 6-month-old (D) posterior rhomboencephalon. Arrowheads indicate examples of regions with perinuclear immunoreactivity. Asterisks indicate regions with filamentous immunoreactivity. Scale bars represent 100 μm in the overviews and 50 μm in the zoom-ins.

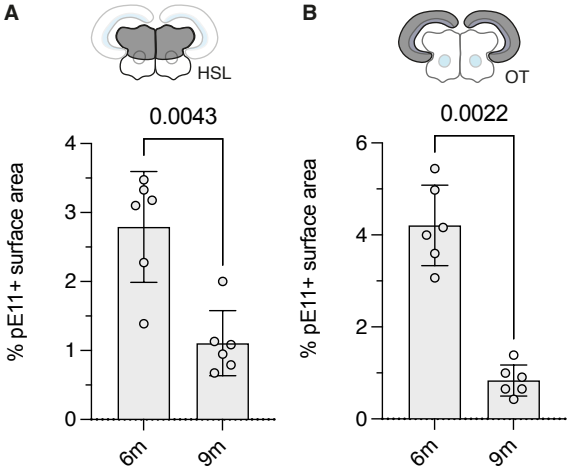

Figure S9. pE11 signal decreases in the turquoise killifish brain between 6- and 9-months of age. (**A, B**) The percentage surface area covered was quantified in an independent cohort of turqoise killifish (strain ZMZ1001) in the (A) hypothalamus superior lobe (HSL) and (B) the optic tetum (OT). Significance was calculated with a Mann-Whitney test.

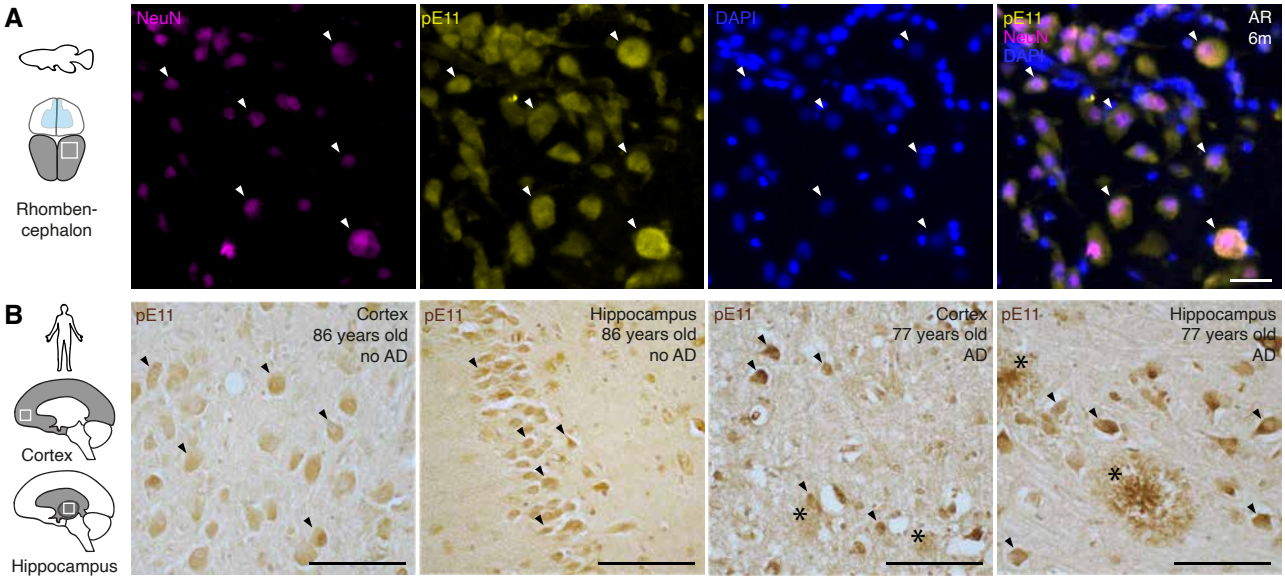

Figure S10. In aged killifish and human brains, pE11 signal predominantly localizes intraneuronally. (**A**) Immunohistochemistry staining in the 6-month-old anterior rhombencephalon (AR) using the pE11 antibody (yellow) and NeuN (Neuronal Nuclei) antibody. Arrowheads indicate colocalizing NeuN and pE11 signals. Scale bar represents 20 μm. (**B**) Immunohistochemistry using the pE11 antibody in two regions of the aged human brain of non-diseased (left) and Alzheimer's diseased (right) brains. Arrowheads indicate intraneuronal signal, the asterisks indicate extracellular plaques. Scale bar represents 100 μm. Images are representative examples of three investigated individuals per condition.

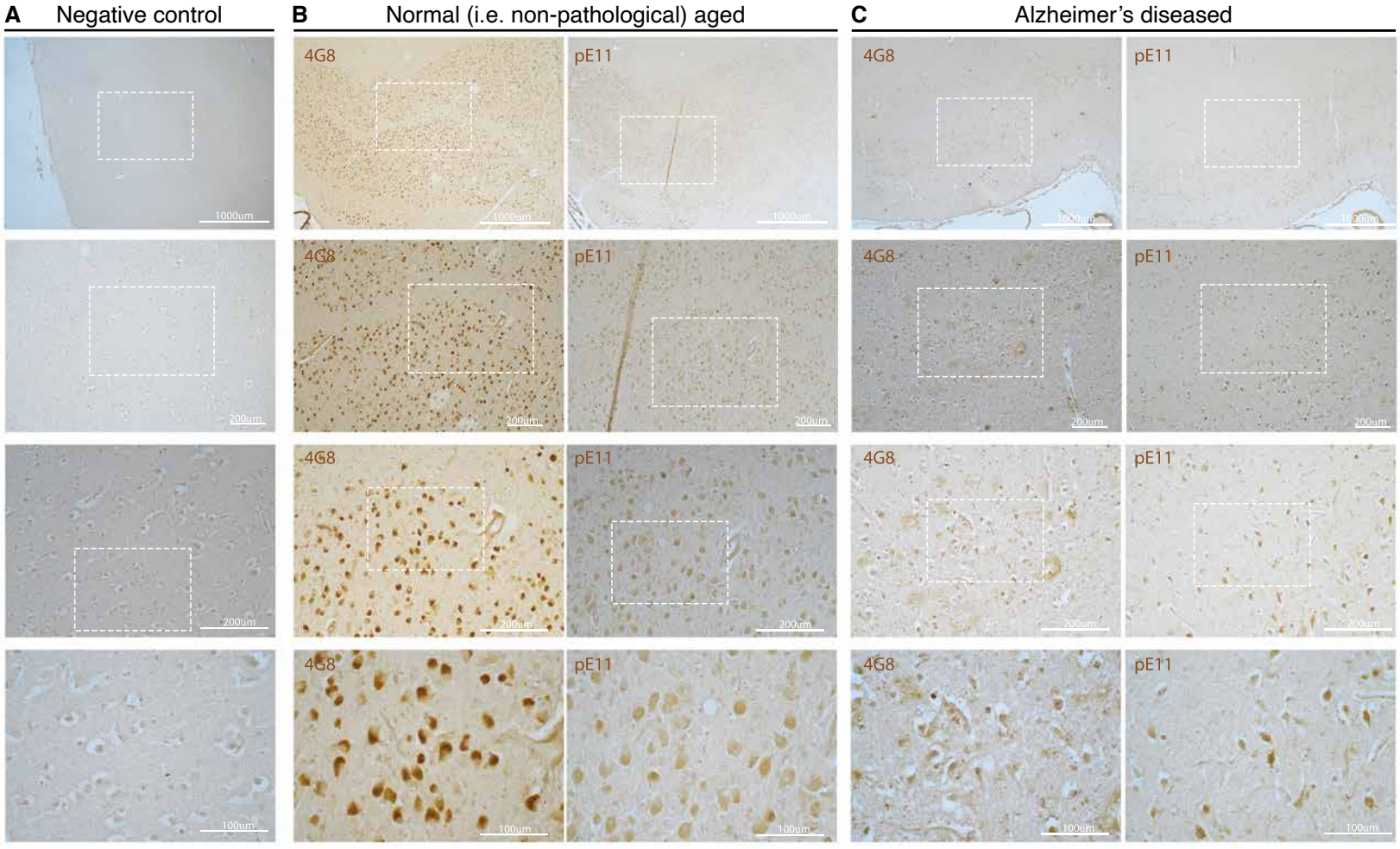

Figure S11. Staining of 4G8 and pE11 in human cortical areas. (**A**) Negative control staining for cortical human areas, realized without the addition of any primary antibody during the protocol. (**B**) Staining for 4G8 and pE11 in cortical areas of a normal (i.e. non-pathological) aged individual (>80 years old). (**C**) Staining for 4G8 and pE11 in cortical areas of an Alzheimer's Disease diagnosed individual (>80 years old). (B, C) These images are representative examples of in total six investigated individuals.

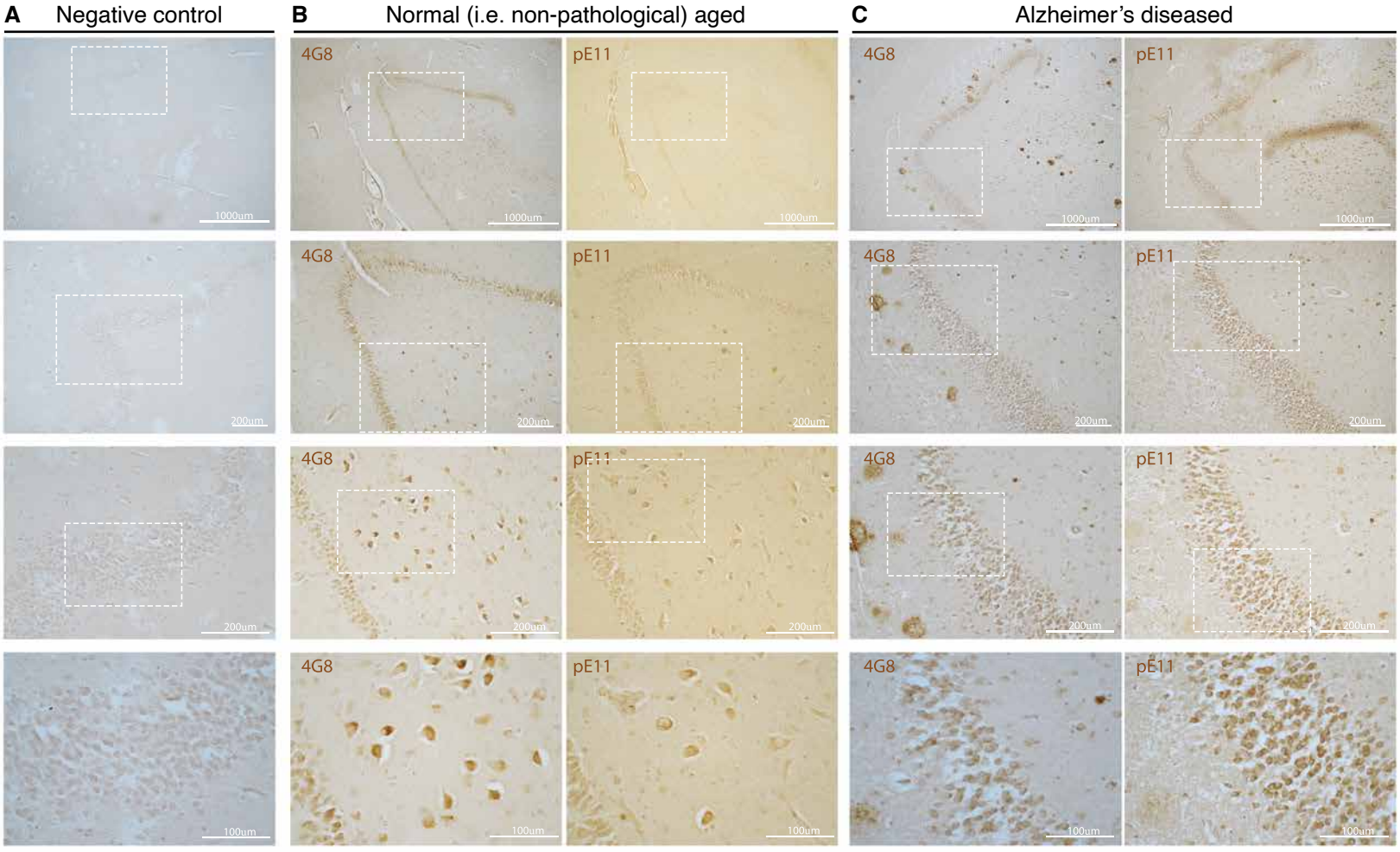

Figure S12. Staining of 4G8 and pE11 in human hippocampus. (**A**) Negative control staining for hippocampal human areas, realized without the addition of any primary antibody during the protocol. (**B**) Staining for 4G8 and pE11 in cortical areas of a normal (i.e. non-pathological) aged individual (>80 years old). (**C**) Staining for 4G8 and pE11 in cortical areas of an Alzheimer's Disease diagnosed individual (>80 years old). (B, C) These images are representative examples of in total six investigated individuals.

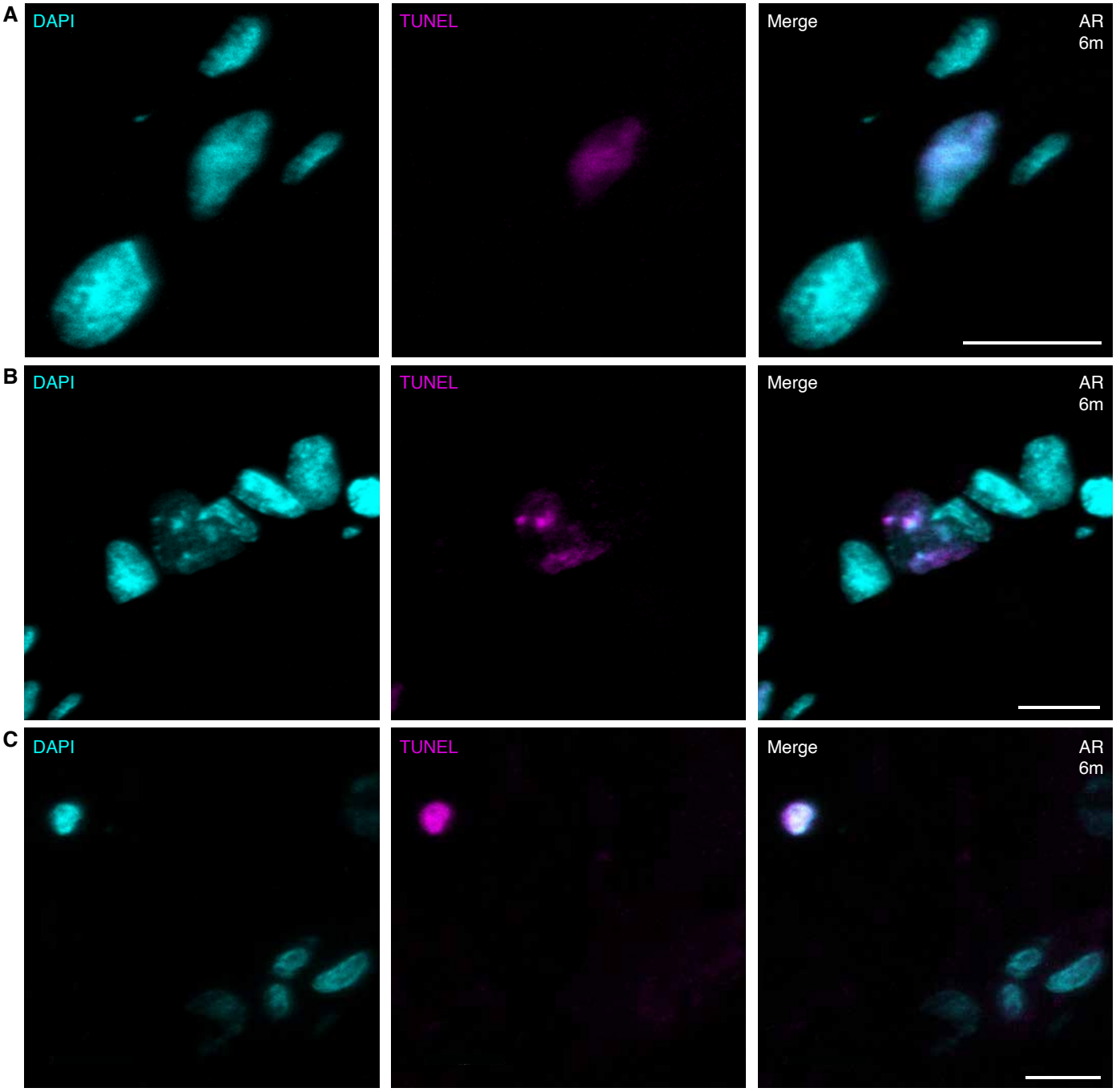

Figure S13. TUNEL staining in the anterior rhombencephalon. (**A-C**) Detection of apoptotic cells in the anterior rhombencephalon (AR) of a 6-month-old turquoise killifish through TUNEL staining. Various staining patterns were identified, including (**A**) visibly intact nuclei, (**B**) fragmented nuclei as well as (**C**) compacted nuclei. Scale bars represent 10 μm.

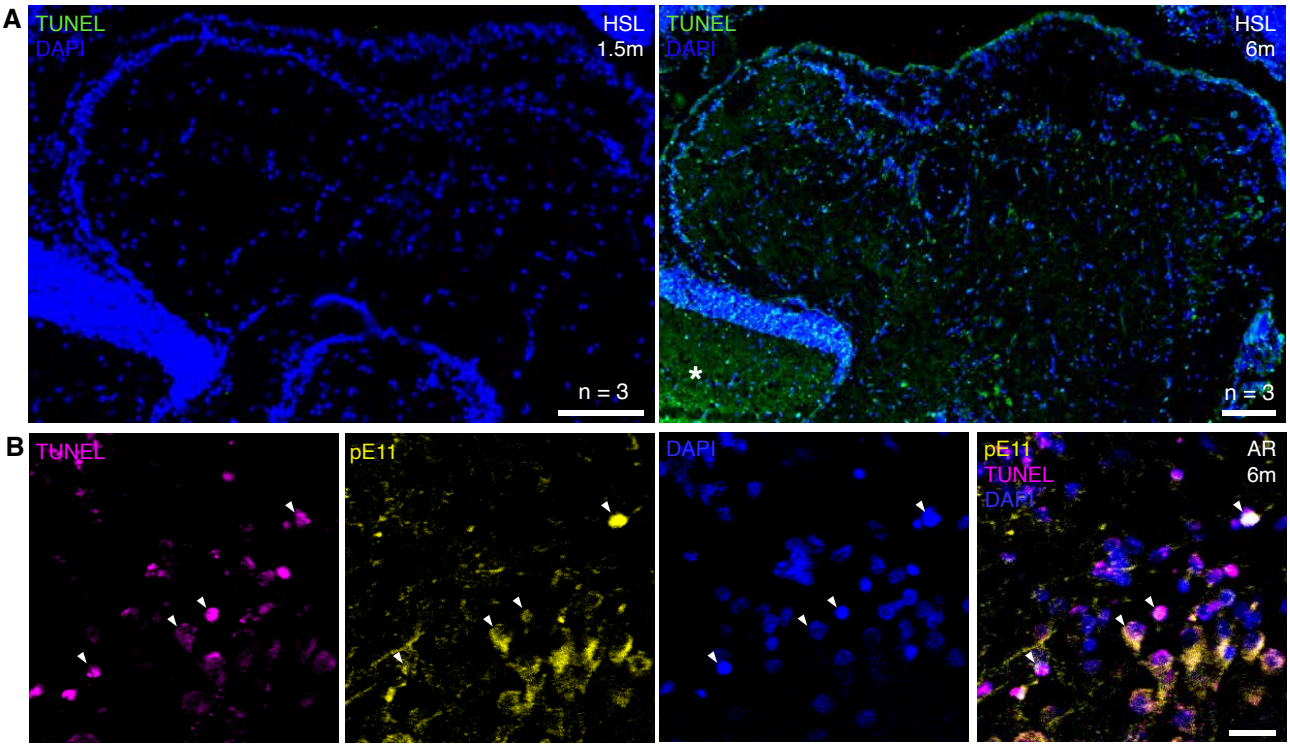

Figure S14. TUNEL staining shows a robust signal in aged turquoise killifish and overlaps with pE11 signal. (**A**) Detection of apoptotic cells in the hypothalamus superior lobe (HSL) of a young 1.5-month-old (**left**) or aged 6-month-old turquoise (**right**) turquoise killifish, visualized through TUNEL staining (green). The asterisk indicates age-related background signal, which was consistent throughout the apical tip of the optic tectum throughout the investigated brain sections of 6-month-old fish. Scale bars represent 100 μm. (**B**) Immunohistochemistry staining using the pE11 antibody (yellow) combined with TUNEL staining (magenta). Arrowheads indicate colocalizing signal. Scale bar represents 20 μm. AR = anterior rhomencephalon.

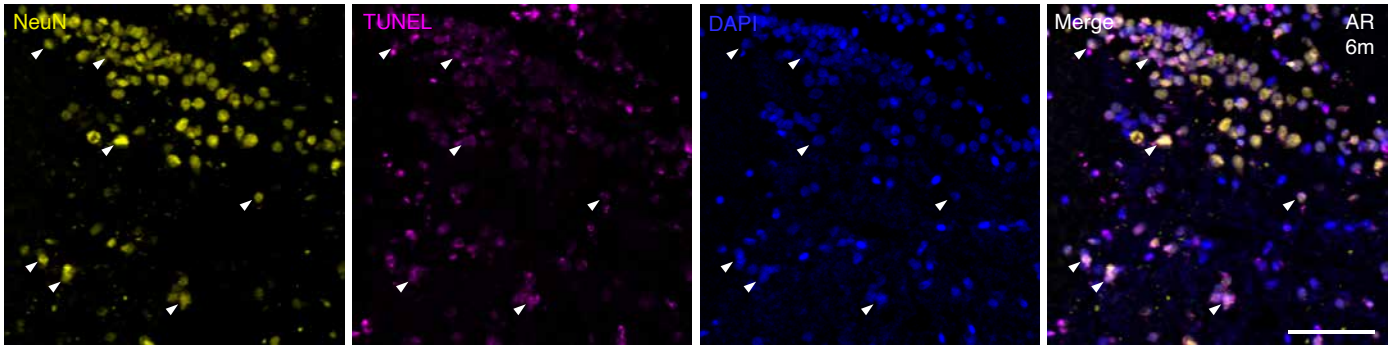

Figure S15. TUNEL staining colocalizes with NeuN in the aged anterior rhombencephalon of the turquoise killifish. (**A**) Immunohistochemistry staining using the pE11 antibody (yellow) combined with TUNEL staining (magenta). Arrowheads indicate colocalizing signal. Scale bar represents 20 μm. The stainings were performed on the anterior rhombencephalon (AR) of a 6-month-old turquoise killifish.

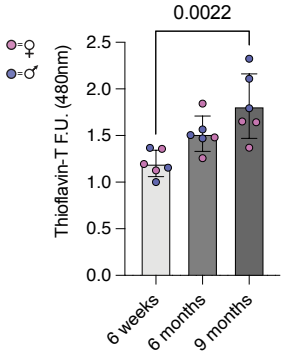

Figure S16. Beta-sheet aggregates accumulate in an age-dependent manner. Thioflavin-T assays were conducted on brain lysates of young, aged and old killifish. Shown values are 480nm emission levels 3 minutes after addition of Thioflavin-T to brain lysates. Values were normalized against the lowest measured value. Significance was calculated using a Mann-Whitney test.

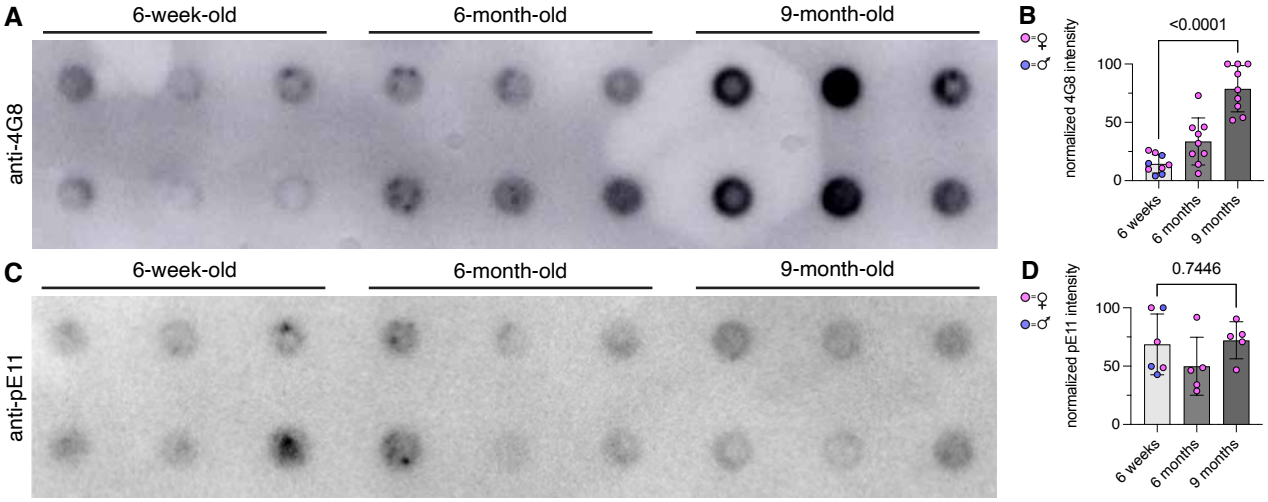

Figure S17. 4G8⁺ peptides aggregate in the turquoise killifish brain in an age-dependent manner. (**A**) Filter retardation analysis of 4G8⁺ aggregates. 100 μg of protein from brain lysates from three individual killifish of each age group was spotted on the filter in duplicates (top/bottom) and probed with an anti-4G8 antibody. (**B**) Quantification of 4G8⁺ signal normalized against the maximum value measured per experiment. Each dot represents the averaged value of three technical replicates per brain. Error bars represent standard deviation. Significance was calculated using a Mann-Whitney test. (**C**) Filter retardation analysis of pE11⁺ aggregates. 100 μg of protein from brain lysates from three individual killifish of each age group was spotted on the filter in duplicates (top/bottom) and probed with an anti-pE11 antibody. (**D**) Quantification of pE11⁺ signal normalized against the maximum value measured per experiment. Each dot represents the averaged value of three technical replicates per brain. Error bars represent standard deviation. Significance was calculated using a Mann-Whitney test.

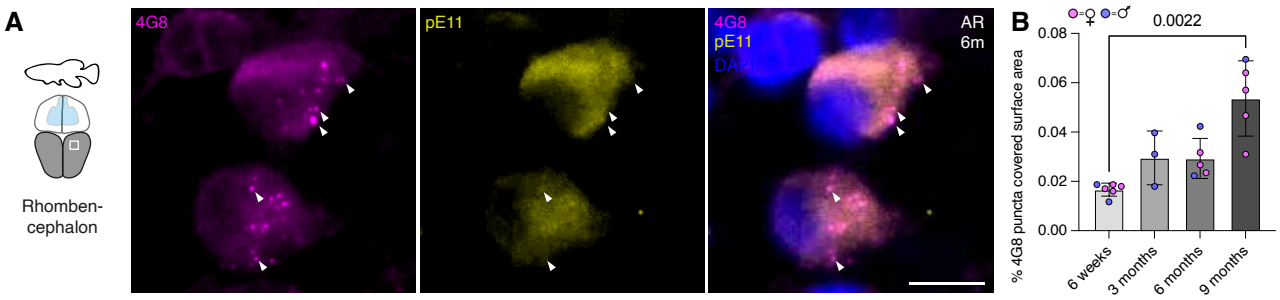

Figure S18. Intraneuronal 4G8⁺/pE11⁻ puncta increase with age in the turquoise killifish brain. (**A**) Immunohistochemistry staining in the 6-month-old anterior rhombencephalon (AR) using the pE11 antibody (yellow) and 4G8 antibody (magenta). Arrowheads indicate 4G8⁺/pE11⁻ puncta. Scale bar represents 10 μm. (**B**) Quantification of the percentage of 4G8⁺-puncta-covered surface area in AR regions at four different ages. Significance was calculated using a Mann-Whitney test. Error bars represent standard deviation.

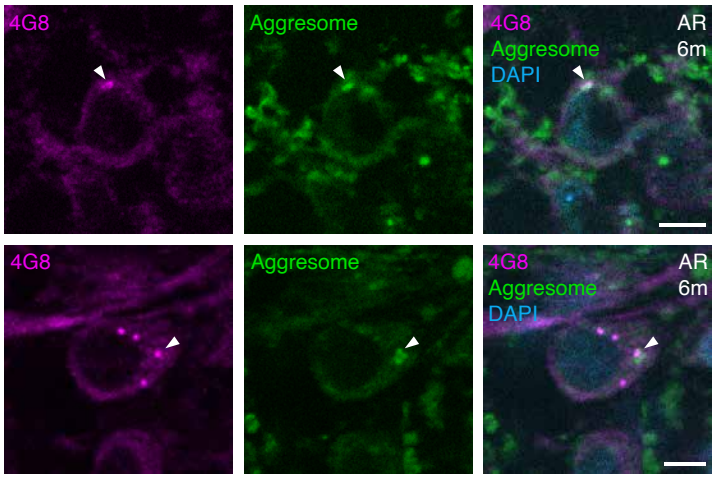

Figure S19. 4G8 puncta partially overlap with Aggresome dye. Two examples of cells in the 6-month-old anterior rhombencephalon (AR) showing an overlap between the 4G8 antibody (magenta) and the PROTEOSTAT Aggresome dye indicating protein aggregates (green). Arrowheads indicate colocalization of Aggresome and 4G8 signal. Scale bars represents 5 μm.

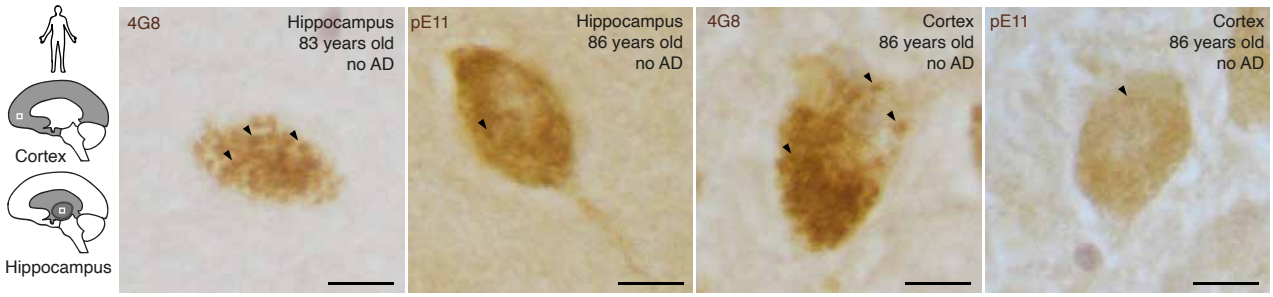

Figure S20. 4G8 staining shows a granulated pattern, which is largely absent in the pE11 staining. Immunohistochemistry using the 4G8 and pE11 antibody in two regions of the non-diseased aged human brain. Arrowheads indicate intraneuronal puncta. Scale bar represents 10 μm.

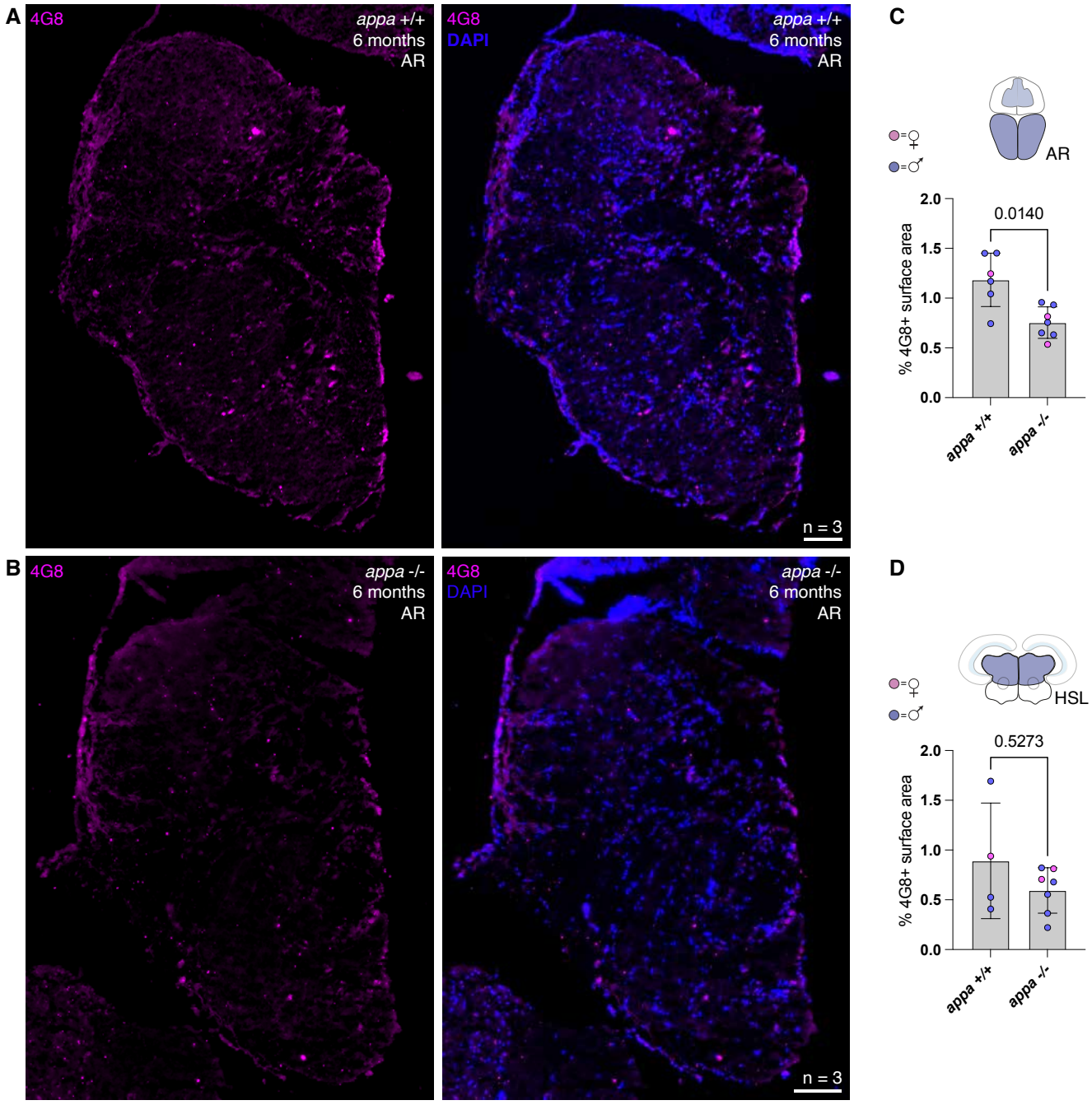

Figure S21. *appa* knock-out reduces 4G8 signal. (**A, B**) Representative immunohistochemistry staining results using the 4G8 antibody (magenta) in the anterior rhombencephalon (AR) of wild-type (A) and *appa* -/- mutant (B) brains. Scale bars represents 100 μm. (**C, D**) Quantification of the percentage of 4G8^{+} covered surface area in the (C) anterior rhomboencephalon (AR) and (D) hypothalamus superior lobe (HSL) of 6-month-old individuals. Significance was calculated using a Mann-Whitney test. Error bars represent standard deviation.

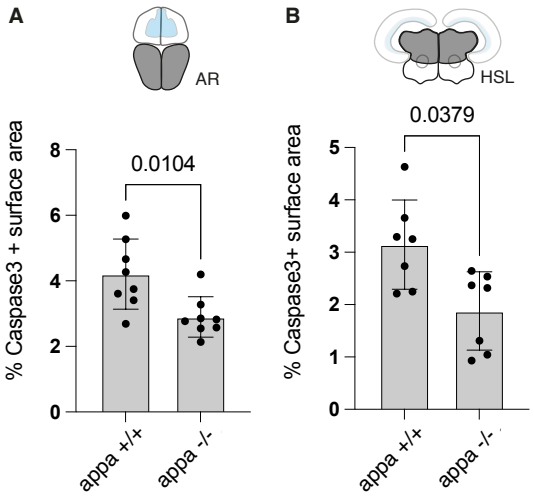

Figure S22. *appa* -/- mutants show a reduction in (pro-)caspase3 covered surface area. (**A, B**) The percentage surface area covered by (pro-)caspase3 was quantified in the (A) anterior rhombencephalon (AR) and (B) hypothalamus superior lobe (HSL) of 6-month-old *appa* -/- mutants and their wild-type siblings. Significances were calculated using a Mann-Whitney test.

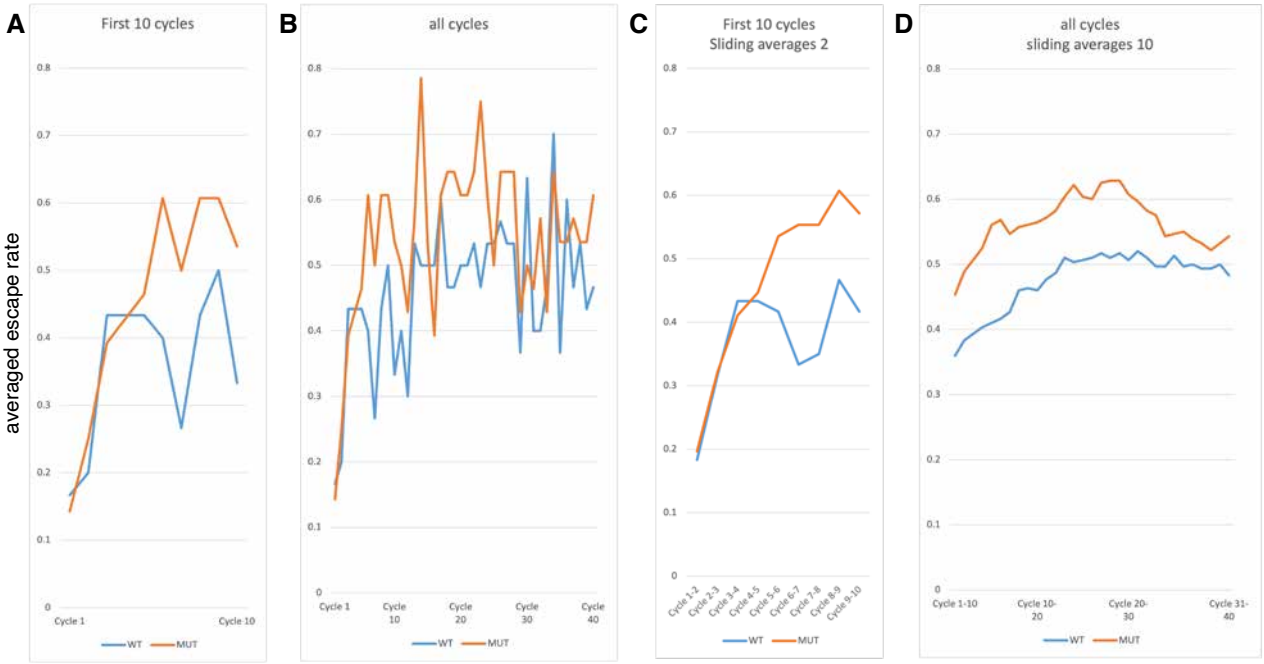

Figure S23. Averaged escape rates of *appa* -/- mutants and their wild-type siblings. (**A, B**) Plot describing the averaged escape rate of 7.5-month-old *appa* -/- mutants (orange, n = 28 fish) and their wild-type siblings (blue, n = 30 fish) across 10 (A) and the full 40 (B) cycles. (**C, D**) Sliding averaged values of the data presented in A and B, using either a sliding average of two (C) or ten (D) to increase the visibility of the general trends.

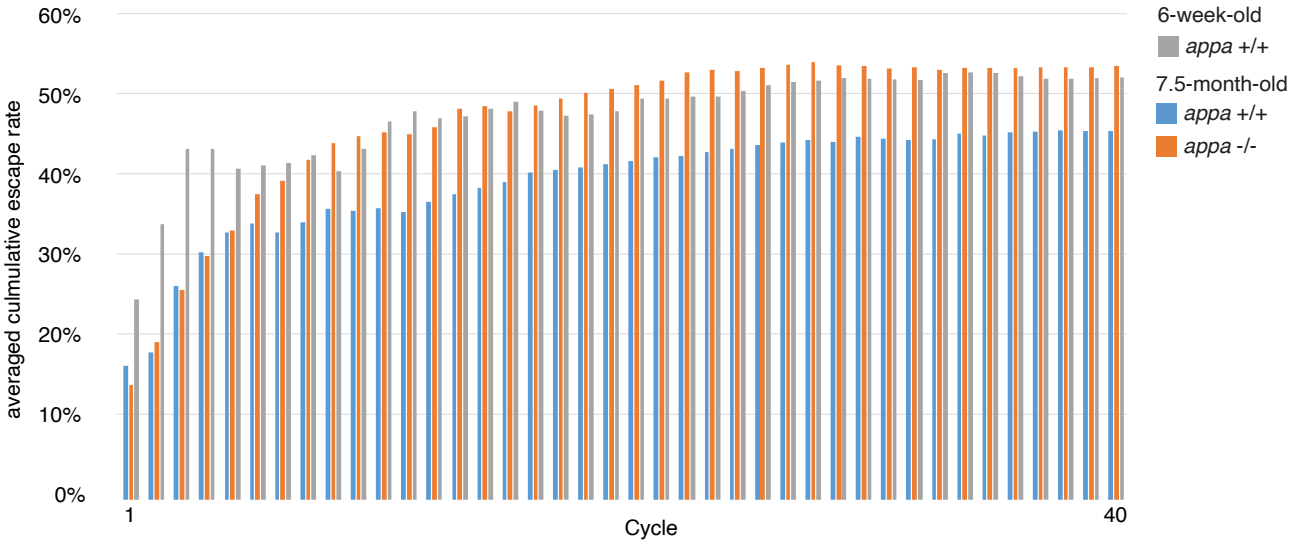

Figure S24. *appa* knock-out mitigates age-related learning deficiency in turquoise killifish. Plot describing the averaged cumulative escape rate of 7.5-month-old *appa* -/- mutants (orange, n = 28 fish) and their wild-type siblings (blue, n = 30 fish) across 40 cycles. In addition, a seperately conducted cohort of 6-week-old individuals has been tested and plotted (grey, n = 16 fish).